Large-scale capture of hidden fluorescent labels for training generalizable markerless motion capture models

Daniel J. Butler, Alexander P. Keim, Shantanu Ray, Eiman Azim[1]

Molecular Neurobiology Laboratory, Salk Institute for Biological Studies, 10010 N. Torrey Pines Road, La Jolla, CA 92037, USA.

[1]Corresponding author (eazim@salk.edu)

Number of Figures: 6

Number of Supplementary Figures: 7

Number of Supplementary Tables: 1

Number of Supplementary Videos: 6

Abstract

Recent advances in deep learning-based markerless pose estimation have dramatically improved the scale and ease with which body landmarks can be tracked in studies of animal behavior. However, pose estimation for animals in a laboratory setting still faces some specific challenges. Researchers typically need to manually generate new training data for each experimental setup and visual environment, limiting the generalizability of this approach. With each network being trained from scratch, different investigators track distinct anatomical landmarks and analyze the resulting kinematic data in idiosyncratic ways. Moreover, much of the movement data is discarded: only a few sparse landmarks are typically labeled, due to the inherent scale and accuracy limits of manual annotation. To address these issues, we developed an approach, which we term GlowTrack, for generating large training datasets that overcome the relatively modest limits of manual labeling, enabling deep learning models that generalize across experimental contexts. The key innovations are: a) an automated, high-throughput approach for generating hidden labels free of human error using fluorescent markers; b) a multi-camera, multi-light setup for generating large amounts of training data under diverse visual conditions; and c) a technique for massively parallel tracking of hundreds of landmarks simultaneously using computer vision feature matching algorithms, providing dense coverage for kinematic analysis at a resolution not currently available. These advances yield versatile deep learning models that are trained at scale, laying the foundation for standardized behavioral pipelines and more complete scrutiny of animal movements.

1 Introduction

One of the key challenges in studying how the body is controlled as it interacts with the environment is simply measuring movement in the first place. Historically, movement studies have employed a wide variety of measurement techniques. Perhaps the earliest and most widely used strategy is qualitative observation, where investigators watch the animal and describe the movements they see[1,2]. This approach has the advantage of not impinging on the subject's behavior, while allowing the investigator to judge which aspects of a complex set of movements are relevant. By the same token, however, human observation is subject to limitations and biases – the observer may not discern subtle features of a movement or may unwittingly fail to record the features relevant to the question being asked.

An important addition to the scientific toolbox was the introduction of marker-based tracking. With this technique, markers are attached to the animal and marker positions are computed from video cameras or other sensors[3-8]. Marker-based approaches afford high accuracy but have several drawbacks. Some animals do not tolerate markers well, and particularly with smaller animals like rodents, it can be difficult to place markers on fine structures like the digits. Furthermore, marker-based tracking is still subject to a degree of human bias, as the investigator must choose where to place the markers well before collecting and analyzing the data.

More recently, as deep learning[9,10] has become a mature technology for extracting information from images and video, markerless tracking methods (e.g., DeepLabCut[11], LEAP/SLEAP[12,13], and DeepPoseKit[14]) have become widely adopted[15-17]. These markerless tracking systems are often used with the following workflow: (1) the investigator records a behavior of interest and manually labels landmarks in a subset of captured video frames; (2) a deep learning model is trained on these labeled frames; (3) the model is used to predict landmark positions in the other frames that have not been manually labeled; (4)

the investigator verifies the labels produced by the model; and finally, (5) if errors are sufficiently rare, analysis proceeds; otherwise the investigator returns to step (1), labels more frames, and trains and applies a new deep learning model with the expectation that a larger training set will reduce the error rate to an acceptable level.

Markerless tracking based on this workflow can produce highly accurate results, sometimes with as few as 100 to 1000 labeled training images. It also carries the advantage that it can be applied post-hoc to video data that was collected without tracking in mind, making it possible, for instance, to quantify the movement of animals in their natural habitats from archival footage. Already, the workflow described above has had a major impact on a variety of fields that study animal behavior, and the applications continue to grow.

Our approach builds on this influential work in markerless tracking and aims to overcome several key obstacles. One obstacle is poor robustness. Although deep learning models trained using the process described can in principle be applied to new experimental setups and visual environments not seen during training, in practice, even small changes, for example in lighting, camera position, or the behavior being measured, often cause accuracy to drop dramatically. Therefore, new setups require new images to be manually labeled and new models to be trained. Another obstacle is that the manual labeling of landmarks has inherent limitations. For one, only landmarks that can be easily identified by humans across images can be labeled. Moreover, the need for human labor increases time and cost, and accuracy is limited by skill level and consistency across human annotators.

Several approaches have recently been proposed for training motion capture models for scientific applications without the need for manual labeling of newly collected data. Some notable methods rely on multi-camera-based 3D reconstruction[18], implanted physical markers[19], or a pre-built 3D model of the target object[20]. We sought to develop an alternative strategy that is non-invasive, does not rely on 3D reconstruction or 3D models, and can enable automated, high-density labeling of the subject. To address these challenges, we developed GlowTrack, an approach to automatically generate large, diverse image datasets along with corresponding landmark labels without the need to manually label video frames. To collect these large training sets, we label the subject with a fluorescent dye that is only excited by wavelengths outside the visible range, and alternately strobe excitation and visible light sources to collect pairs of images in which the dye is either visible or absent. Image data is then processed and used to train a model that can detect landmarks on animals that do not have any fluorescent label applied. Primarily due to the dramatic increase in data set size and visual diversity, deep learning models trained with this approach are robust enough to operate in different contexts, giving experimenters more flexibility to change their setups without labeling additional images or training new models.

We present two pipelines for turning fluorescent labels into trained landmark trackers. The *serial labeling* pipeline enables reliable tracking of specific landmarks of interest. The *parallel labeling* pipeline enables tracking of an arbitrary number of automatically selected landmarks, eliminating the need for the investigator to pre-select a small number of landmarks *a priori*, thereby reducing bias and increasing coverage (**Fig. 1**). Ultimately, more sensitive, reliable, and comprehensive methods to capture and quantify movement could have wide-ranging use in experimental science, ethology, clinical diagnosis, robotics, and augmented reality.

2 Results

Our approach to generating labeled images is based on applying hidden fluorescent fiducials to body regions of interest, inspired by the use of fluorescent dye to generate ground truth data for other applications[21]. Here, we establish the hidden fluorescence approach for deep learning-based pose estimation and develop several innovations to optimize it for generating high quality pose labels at large scale. We describe two different variants of our labeling approach, each tuned for different performance characteristics (**Fig. 1**).

The first variant, which we call *serial labeling*, can be used to label nearly any landmark regardless of the shape or texture of the surface (**Fig. 1a**). In the serial labeling approach, a single landmark is labeled

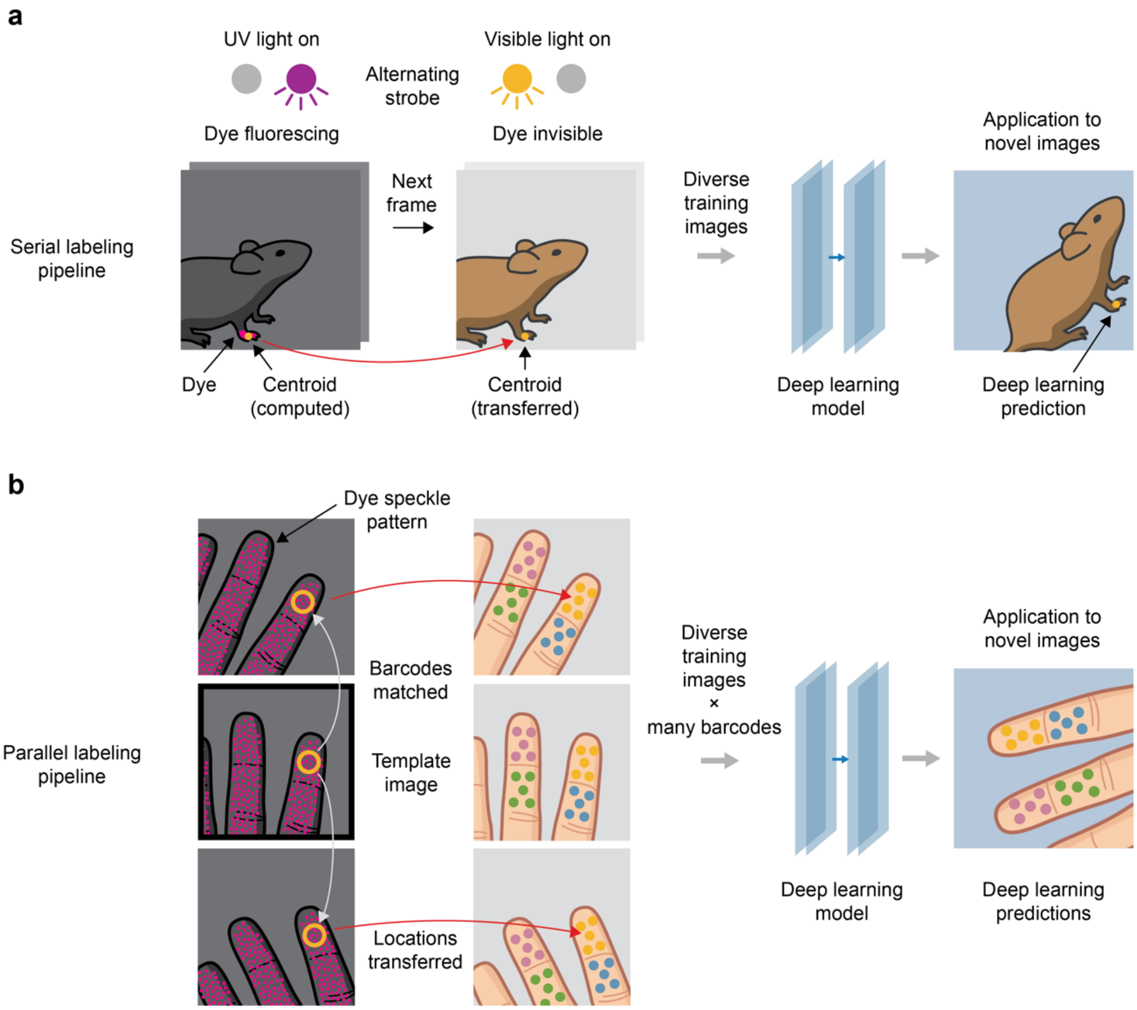

Fig. 1. Hidden fluorescent labels for training versatile landmark detectors. a) In the serial labeling pipeline, a target landmark is marked with a fluorescent dye. UV and visible illumination sources are strobed alternately, switching the dye between fluorescing and invisible states. The centroid of the dye region is computed in post-processing and is used as a landmark label for the subsequent visible light frame (red arrow), in which dye is invisible (see **Supp. Fig. 1**). In this way, a large, automatically labeled image dataset is generated and used to train a deep learning model to predict landmark locations in novel images. **b)** In the parallel labeling pipeline, many landmarks are labeled simultaneously with a fluorescent speckle pattern where local neighborhoods form distinctive visual barcodes. A small number of images are selected as templates (black outline), and labels are propagated from template images to all other images that contain matching barcodes (gray arrows) and then transferred to the corresponding visible light images (red arrows). These labels are then used to train a deep learning model to predict landmark locations in novel images.

with the fluorescent dye, and the data synthesis process is repeated for each landmark one wishes to label. As proof-of-concept, we use the serial labeling procedure to train a robust deep learning model for tracking the hand of the mouse and evaluated its accuracy on challenging image data from novel experimental setups and behaviors. We further improve performance by using real-time feedback from the model to optimize camera settings and achieve better accuracy.

The second variant, which we call *parallel labeling*, expands this concept to the labeling of an unbounded number of landmarks simultaneously (**Fig. 1b**). In the parallel labeling approach, dye is applied in a random speckle pattern, yielding hundreds to thousands of visually identifiable local regions, or *visual barcodes* (in analogy to the synthetic nucleic acid barcodes used in biological applications[22-24]), that can be matched across images. We apply this procedure to the human hand, training a deep learning model to track many landmarks in parallel at a density of coverage decided by the user. Our approach is not restricted to tracking the human hand, an active research area with an extensive literature[25-28]; rather, we use the hand as proof-of-concept that our data generation technique can be used to quickly train a versatile model that tracks many points on a complex, articulated object.

The two variant approaches share many attributes in common, so for clarity of exposition, we first describe serial labeling and associated experiments, and then describe parallel labeling as an extension.

2.1 Serial labeling with hidden fluorescent dye

Overview

In the serial labeling pipeline (**Fig. 1a**), a single target landmark is marked with an ultraviolet (UV) fluorescent dye using a fine brush or felt-tipped marker. We use UV fluorescent dye because of its commercial availability, but, in principle, dyes that fluoresce at other wavelengths could be used. UV and

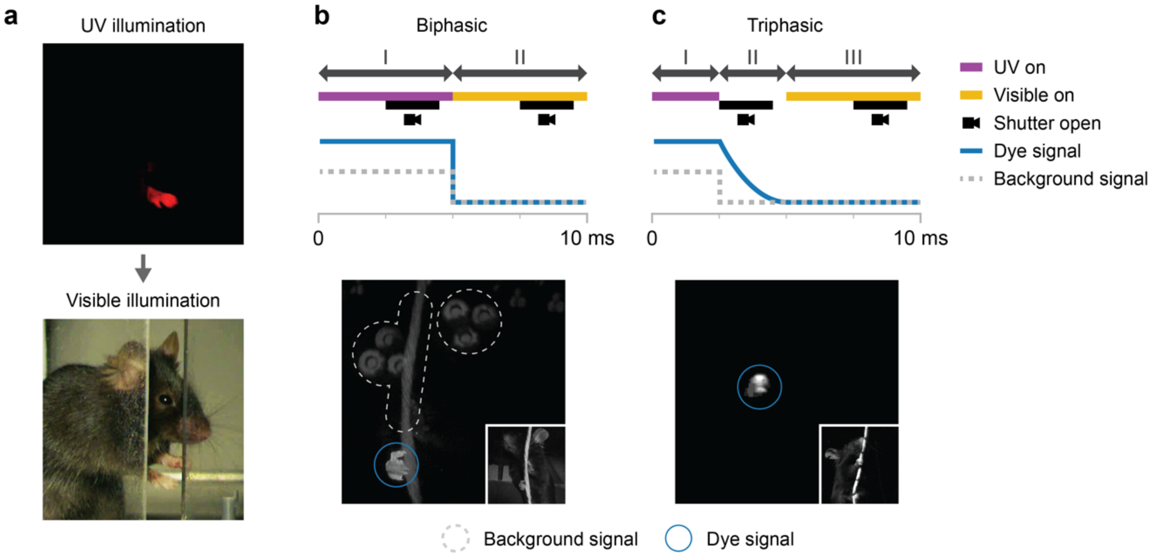

Fig. 2. Triphasic illumination with delayed-decay fluorescent dye eliminates background signals. a) Adjacent video frames captured under UV illumination (top) and visible illumination (bottom). **b)** Biphasic illumination and image capture scheme (top), in which the UV image is captured while the scene is UV-illuminated. Example UV image from the biphasic scheme (bottom) showing two major sources of background signal (fluorescence of background objects, and broadband light from the UV source; dashed outlines) that make the dye region (blue circle) difficult to isolate. **c)** Triphasic illumination and image capture scheme (top), in which the UV image is captured after UV illumination has been turned off. A dye with a longer temporal decay constant is required. Example UV image from the triphasic scheme (bottom) showing that background signal is eliminated. Insets in **b** and **c** show corresponding visible illumination images.

visible illumination sources are strobed alternately, switching the dye between fluorescing and invisible states (**Supp. Video 1**). The centroid of the dye region is then computed from the UV-illuminated images in post-processing (**Supp. Fig. 1**). The dye centroid from each UV frame is used as a proxy label for the subsequent visible frame in the video, thereby transferring each UV-computed centroid to a visible image. This transfer procedure is justified because, at high video frame rates, the discrepancy between the landmark locations in adjacent UV and visible frames is negligible (**Fig. 2a** and **Supp. Fig. 1**; the frame rate was 200 Hz for the experiments reported here, well within the range of standard machine vision cameras). In this way, a large, diverse, and accurately labeled image dataset can be generated without the need for manual labeling of any frames. In the final step of the pipeline, this large dataset undergoes a process of data augmentation (see Methods) while it is used to train a deep learning model that can be used to predict landmark location in novel images in which no dye is present (**Supp. Fig. 1**).

Illumination

The relative timing of the illumination phases and image capture is important. In the simplest implementation of serial labeling, which we call biphasic illumination, each fluorescence image is captured while the UV source is actively illuminating the dye, after which the illumination is switched to visible light for visible image capture (**Fig. 2b**, top). Although this scheme is intuitive, the UV source is on during image capture, allowing light from the UV source to leak into the camera, decreasing the signal-to-noise ratio and making the dye more difficult to localize during post-processing (**Fig. 2b**, bottom). Mounting an optical low-pass filter onto each camera reduced background signal from the UV source but did not completely eliminate it, likely because the UV LEDs emit a broad spectrum that includes some wavelengths in the visible range.

A more serious problem that could not be solved with spectral filtering was the natural fluorescence of objects in the scene (**Fig. 2b**, bottom). To eliminate natural scene fluorescence, we developed a second image capture configuration that we call triphasic illumination. This scheme is based on our observation that the natural fluorescence in the scenes we captured had a short temporal decay constant (likely on the order of less than 1 microsecond). We reasoned that if we use a dye with a longer temporal decay constant, the UV source can be turned off just prior to image capture, allowing natural fluorescence to subside while the dye continues to fluoresce[†] briefly (**Fig. 2c**, top). This approach essentially eliminates both light leakage from the UV source and natural scene fluorescence (**Fig. 2c**, bottom). Moreover, because the UV source is not active during capture of UV images, there is no need for a low-pass filter to block UV light, resulting in a cheaper and simpler optical setup. The triphasic

[†] Longer decay processes are typically mediated by a mechanism known as *phosphorescence*, but we use the term *fluorescence* generically to refer to any decay process.

illumination approach enabled us to capture very large image sets with high signal to noise and without the need for manual removal of images with natural scene fluorescence. All experiments that follow were performed using triphasic illumination.

In image post-processing, we then compute label positions from the raw UV images (**Supp. Fig. 1**). First, the dye must be identified in the UV image. Owing to the very low background noise produced by the triphasic illumination scheme, we found that simple thresholding is sufficient to produce an accurate binary mask delineating the dyed region. Next, the binary mask is cleaned using morphological operators[29], which we use to smooth edges and eliminate small holes and islands. Finally, the centroid (i.e., the center-of-mass) of the dye region is computed and stored as the label for the subsequent visible frame. For all frames in which the dye mask is empty after the cleaning step (e.g., scenes in which the landmark is occluded), the landmark position is recorded as absent and retained in the training set, as negative examples are important for effective model performance.

Even at high frame rates, on the rare occasions in which movements are very rapid, there can be a small discrepancy between the position of the generated label and the true landmark position on the subsequent frame. To determine if these cases present a problem, we used linear as well as bicubic interpolation to fill in the landmark position for each visible frame based on neighboring UV frames. However, we found that this interpolation scheme generally did not improve the final performance metrics (see sections 2.3 and 2.4), and therefore it was not used in the experiments that follow.

After synthesizing a labeled set of images, the final step in the serial labeling pipeline is to train a deep learning model to perform landmark detection. For the experiments reported here, we used the DeeperCut model[30], but other architectures could also be used. One issue that must be addressed is how to treat absent landmarks. Depending on the model architecture and the desired prediction behavior, different approaches could be used. The DeeperCut model produces a confidence map for each landmark.

To account for absent landmarks, we configured the training procedure to encourage the model to produce an all-zeros confidence map for images in which the landmark was absent. The confidence map thus serves the dual purpose of encoding positional uncertainty and the probability that a landmark is present at all. To produce a final set of predictions from the model, we consider any predicted labels with confidence below a given threshold to represent landmarks that are absent (our evaluation metrics do not require a fixed threshold, but rather measure performance over all possible thresholds; see section 2.3).

2.2 Increasing image diversity

Fluorescence-based labeling can generate hundreds of labeled images per second, but those images tend to be highly redundant; the pose of the target does not change dramatically from one frame to the next, and the camera angle and lighting conditions do not change at all. In preliminary experiments we found that deep learning models trained on these images only produce accurate predictions in a limited range of visual environments.

To train a model with more visual diversity in the training data, we built a hemispherical dome with eight cameras and nine independently controlled light sources (**Fig. 3a-c** and **Supp. Video 2**). The dome was assembled from custom 3D-printed parts and some off-the-shelf components (see Methods). Half of the cameras were monochrome and half were color, while four of the nine light sources were red and the others were white. Crucially, we designed custom LED holders along the periphery of hexagonal panels to ensure that UV illumination was omnidirectional and isotropic, avoiding UV shadows during video capture that would cause the dye to fail to fluoresce in some frames (**Fig. 3b**). Using a dome rather than a rectilinear system also allowed us to position the illumination sources at a unform distance from the target, further reducing UV anisotropy.

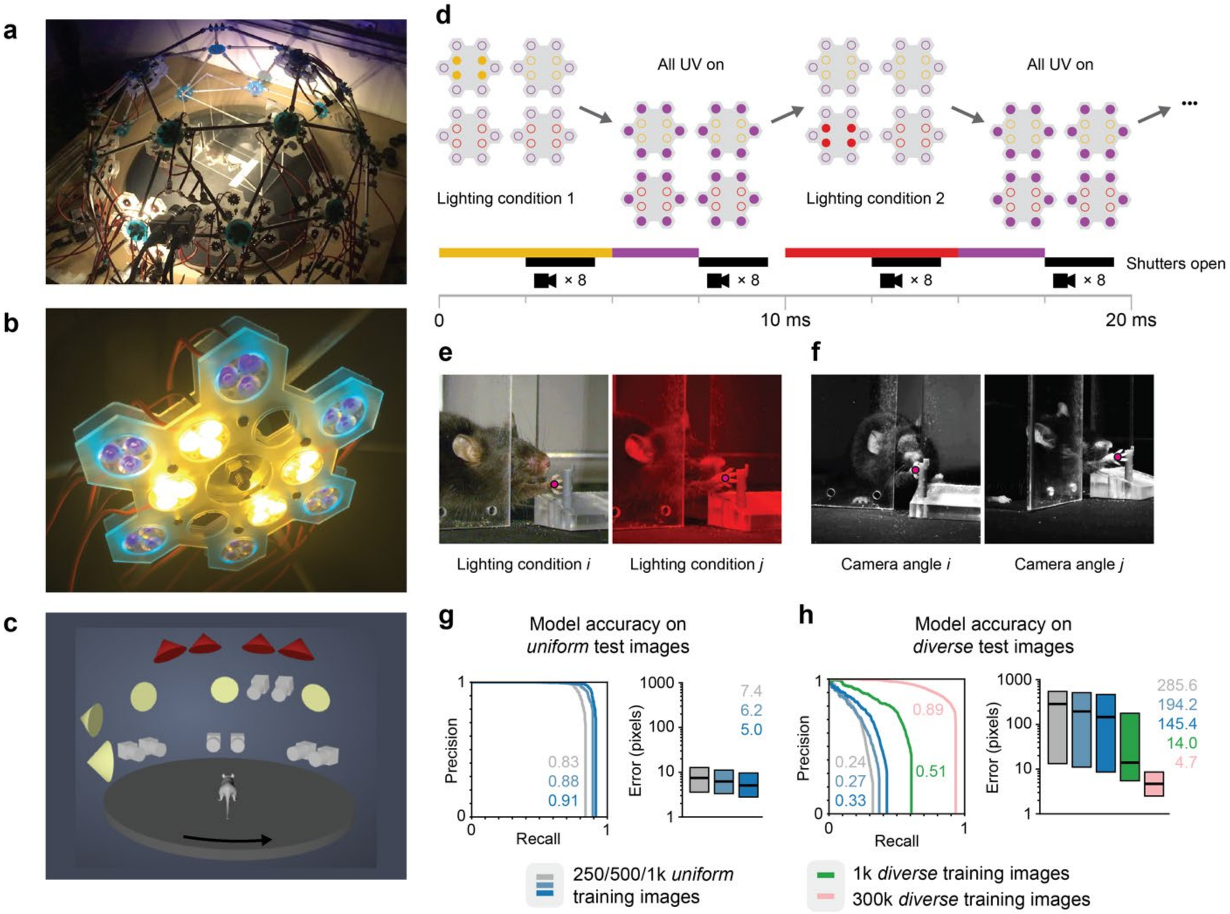

Fig. 3. A large, diverse training set derived from fluorescence imagery yields improved performance. a) A custom-made geodesic dome with eight cameras and nine LED clusters. **b)** Each LED cluster contains visible LEDs at the center and UV LEDs at the periphery. **c)** The spatial configuration of lights (5 white and 4 red) and cameras (4 monochrome and 4 color). Each light module is activated independently to produce images with different illumination angles. The platform inside the dome rotates to generate diverse azimuthal angles. **d)** Sequence of illumination and camera triggers during video capture. All UV LEDs are triggered simultaneously to eliminate UV shadows. UV and visible illumination are activated alternately. During the visible illumination phase only a single cluster (white or red light) is active, the active cluster cycling sequentially. All 8 cameras capture simultaneously. **e)** Two images captured under different lighting conditions on adjacent frames. Landmark labels (magenta dots) are derived from the corresponding fluorescence images (not shown). **f)** Two images captured simultaneously from different cameras, increasing angular diversity in the training data. **g)** Precision-recall curves (left; numbers indicate area under the curve) and pixel error quartile plots (right; lines and numbers indicate median, boxes indicate 25th and 75th percentiles) of models trained on a single lighting condition and camera angle (uniform), and tested under the same conditions. High accuracy is achieved with only a modest number of training images (250-1000). **h)** When tested under diverse lighting conditions and camera angles, the accuracy of models trained on the uniform image set decreases significantly. Training on a diverse (multiple cameras and lighting conditions) but small set of images (green, 1000 images) shows some increase in accuracy but does not fully rescue performance. Training on 300k diverse images results in significant improvements (pink) that are comparable to results in **g**.

By activating only one directional light source at a time during each successive frame, we produced images that exhibited a richer variety of lighting conditions (**Fig. 3d,e**). In addition, by capturing video from multiple cameras, we both increase the angular diversity of the data and collect more images per unit time (**Fig. 3f** and **Supp. Fig. 2**). Finally, animals performed several different behaviors on a circular platform that could be rotated throughout image capture, further contributing to image diversity (**Fig. 3c** and **Supp. Fig. 2**).

2.3 Evaluating manual versus fluorescence-based labeling

A key question we sought to answer was whether a large, diverse training set derived from hidden fluorescent labels could be used to train deep learning models that are more robust to varying visual contexts than the standard manual labeling pipeline, which often yields models that are hyper-specialized to a particular setting. To that end, we collected a large dataset of mouse behavior using the fluorescence pipeline described above to label one hand on the mouse. The full dataset contained 380,000 images representing eight camera angles, nine lighting conditions, and three behaviors: reaching for a pellet (captured at 100 UV/visible image pairs per second, with 5 ms delay within each pair), pulling a string (also 100 image pairs per second), and moving freely in an enclosure (2 image pairs per second) (**Supp. Fig. 2**). This dataset was divided into 300,000 training images and 80,000 held-out test images. Note that unlike most evaluations in prior work, our training and test images are drawn from non-overlapping video clips, increasing the degree of difficulty and more accurately reflecting the challenge of domain generalization.

To emulate the kind of models commonly trained using the manual labeling workflow, we created subsets of the training and test sets respectively, both containing imagery from only a single camera and single lighting condition. We call these subsets *uniform* because they reflect a single experimental setup in fixed imaging conditions. Likewise, we call the full datasets, with their variety of camera angles and lighting conditions, the *diverse* sets. We trained three models with 250, 500, and 1000 images each sampled from the *uniform* training set. Because these quantities are commensurate with those typically used for manual labeling[11], we refer to these models as having been trained in the manual regime. The *uniform* dataset had an approximate image scale of 100-110 pixels per centimeter, and the *diverse* dataset had an approximate image scale of 50-110 pixels per centimeter.

To quantify model performance, we compared landmark predictions produced by the models to ground truth landmark locations using several metrics. *Pixel error* is defined as the distance between the predicted landmark location and its corresponding ground truth location. An on-target prediction is a prediction satisfying three conditions: the corresponding ground truth label is not absent (i.e., the landmark is visible); the prediction confidence is above a certain threshold; and the pixel error is below a certain threshold (5% of image width). *Recall* is defined as the number of on-target predictions divided by the total number of images in which the landmark is visible. *Precision* is defined as the number of on-target predictions divided by the total number of predictions with confidence above threshold. *Precision-recall* (PR) *curves* are the set of 2D points traced out by computing precision and recall for all possible confidence thresholds. Area under the curve (AUC) is the integral of a PR curve; its maximum value is 1, with larger values indicating better accuracy.

In agreement with previously published results[11], we found that models trained on images from the *uniform* set achieved high accuracy when tested on held-out test images also drawn from the *uniform* set, even when the number of training images was less than 1000 (i.e., in the manual regime) (**Fig. 3g**). For instance, the model trained on 1000 images achieved an AUC of 0.91 and a median pixel error of 5.0. Next, to assess the robustness of these models to varying conditions, we tested them on held-out test images from the *diverse* set. We found that accuracy decreased substantially. For the model trained on 1000 images, AUC dropped from 0.91 to 0.33 and median pixel error increased from 5.0 to 145.4 (**Fig. 3h**). These results support the idea that models trained in the manual regime are sensitive to imaging conditions.

A natural question is whether this sensitivity to conditions is due to the small size of the training set or its lack of visual diversity. Therefore, for comparison, we also trained a model with 1000 images drawn from the *diverse* set and evaluated this model on the *diverse* test set (**Fig. 3h**). While this model achieved better accuracy (AUC = 0.51; median pixel error = 14.0), these results still represent a significant drop in performance compared to the models trained and evaluated on the *uniform* dataset. This result suggests that increasing training image diversity is not sufficient to rescue performance on a diverse test set; for a model to perform well under variable conditions, more training data is required. To test this idea, we trained a model on a large subset of the *diverse* set containing all 300,000 images that were not part of the held-out test set (**Fig. 3h**). When evaluated on images drawn from the *diverse* test set, this model was far more accurate (AUC = 0.89; median pixel error = 4.7), comparable to performance when *uniform* training and test data are used (**Fig. 3g**).

Evaluating model performance on a set of test images requires ground truth labels to serve as a basis of comparison for the labels produced by the model. In all the above evaluations, we used fluorescence-derived labels as ground truth. To confirm that fluorescence-derived labels are indeed a valid source of ground truth, we manually labeled a subset of the *diverse* test set and repeated the same evaluation with these manual labels serving as ground truth (**Supp. Fig. 3a**). The results did not change, confirming that fluorescence-derived labels can serve as valid ground truth for evaluation. Finally, we evaluated all models using the object keypoint similarity mean average precision (OKS-mAP) metric, another standard performance measure that takes into account object scale and annotation uncertainty[31], revealing similar results (**Supp. Table 1**). Together, these findings indicate that training on a large-scale dataset generated using our automated fluorescence labeling technique can achieve robustness to variable imaging conditions that is not achieved by models trained on smaller and less diverse datasets typical of manual labeling.

2.4 Robustness across experimental setups

While the *diverse* set contains a wide variety of imaging conditions, the true heterogeneity seen across behavioral setups and laboratories is not sufficiently represented. To assess the versatility of this labeling approach more rigorously, we next examined the extent to which a model trained on a large-scale fluorescence dataset could generalize to visual contexts completely different from the one it was trained on. We collected a *challenge* dataset from archival video (monochrome and color) of mice performing six different behaviors in six different environments across two laboratories (**Fig. 4a**). This dataset has an approximate image scale of 30-160 pixels per centimeter. To acquire ground truth labels for evaluating prediction accuracy, a subset of frames from the *challenge* set were manually labeled by human annotators.

When evaluated on the *challenge* set, the model trained on 1000 images from the *diverse* set performed poorly (AUC = 0.21; median pixel error = 221.9), while training with the full set of 380,000 images from the *diverse* set resulted in a boost in accuracy, doubling AUC and reducing pixel error by a factor of 9 (AUC = 0.52; median pixel error = 24.3) (**Fig. 4e**). Despite this increase in accuracy by increasing the quantity of training data, we sought to further improve performance. Given the wide variability in image scale across the *challenge* set, we hypothesized model accuracy could be improved by rescaling the dimensions of each test image prior to processing by the trained model, thus changing the

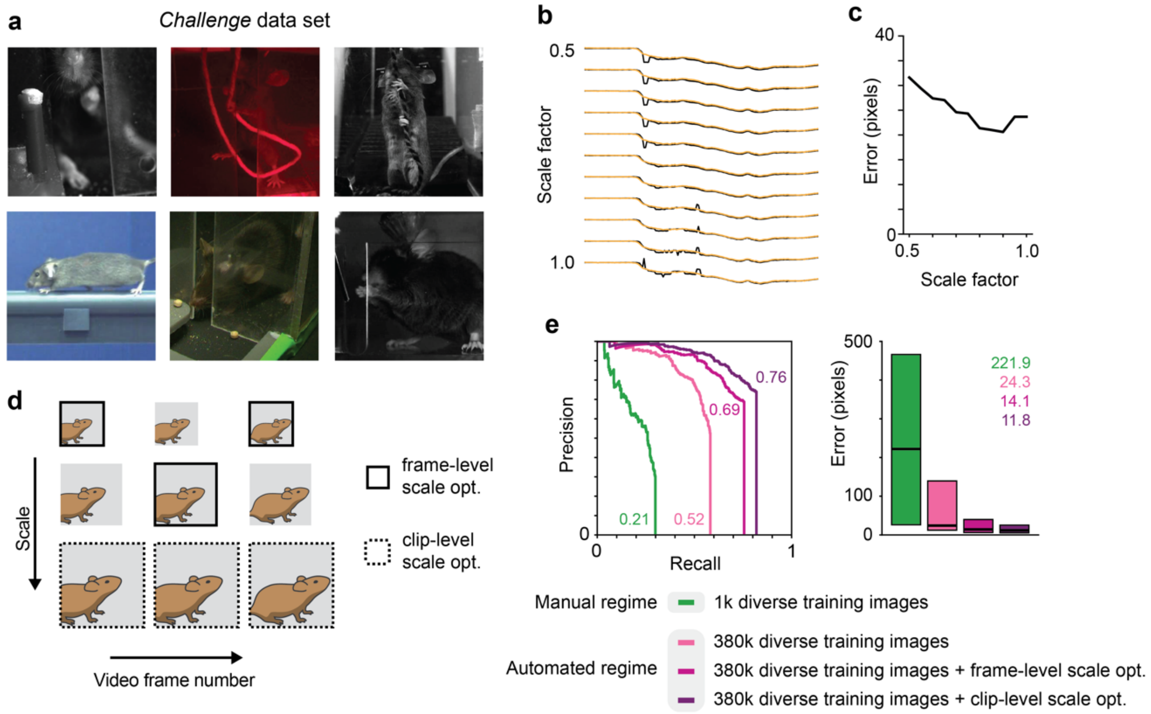

Fig. 4. Landmark detection on novel setups using test time scale optimization. a) Sample images from a *challenge* dataset, collected from various experimental setups. **b)** Hand trajectories produced by a trained deep learning model on a video clip from the *challenge* set (only x values shown). Each row represents a different spatial scale factor applied to the test clip prior to landmark detection. Each yellow curve represents the true, manually labeled trajectory, and each black curve represents the trajectory estimated by the model. Deviations in the black curves indicate prediction errors. **c)** Model prediction error in pixels versus scale factor. The model exhibits a preferred scale. **d)** Two schemes for test time scale optimization: frame-level (solid) and clip-level (dashed). In frame-level optimization, each frame receives its own scale factor. In clip-level, all frames share the same scale factor. **e)** Precision-recall curves (left) and pixel error quartile plots (right) for the different types of scale optimization compared to performance with no scale optimization. Clip-level scale optimization achieves the highest performance.

apparent size of the animal to more closely match that seen in the training data. Testing this idea, we found that applying a range of different pre-scaling factors (0.5 to 1.0) to the frames of a test clip before feeding them to the deep learning model resulted in different predicted hand trajectories of varying accuracy (**Fig. 4b,c**; yellow curves represent ground truth hand trajectories; black curves represent model predictions, while bumps are indicative of model errors). The fact that model predictions tend to be most accurate for a particular, but unknown, pre-scaling factor that varied by video clip motivated us to implement a process of scale optimization at test time to improve accuracy.

The goal of scale optimization is to select the image pre-scaling factor that causes the model to produce predictions that exhibit minimum pixel error. However, in the general case, ground truth labels are not available at the time the model is applied to a video clip, since it is precisely when labels are missing that the model is needed; therefore, pixel error cannot be computed directly. To address this issue, we decided to optimize confidence values as a proxy metric instead. Scale optimization with the confidence metric can be applied independently to each frame (frame-level scale optimization), or it can be applied uniformly to an entire video clip such that all frames share a single scale factor (clip-level scale optimization) (**Fig. 4d**). Both styles of scale optimization yielded significant accuracy improvements over the raw model output. A model trained on the full *diverse* set (380,000 images) and tested with *frame-level* scale optimization achieved an AUC of 0.69 and a median pixel error of 14.1, while *clip-level* scale optimization achieved an AUC of 0.76 and a median pixel error of 11.8, well above performance with no scale optimization applied (**Fig. 4e** and **Supp. Video 3**). As above, the OKS-mAP metric produced similar results (**Supp. Table 1**). It was somewhat surprising that clip-level scale optimization consistently produced more accurate results than frame-level optimization. We speculate that this may be due to the fact that maximizing confidence rather than minimizing true error introduces some noise into the value of the optimal scale, while averaging confidence over all frames tends to reduce the magnitude of this noise term.

To further explore the impact of training set characteristics, we performed a series of ablation experiments, reducing the number of camera angles, lighting conditions, and overall training dataset size, each independently. We found that modifying any of these parameters impacts performance, with training dataset size having the largest impact (**Supp. Fig. 3b**). We also note that several established temporal smoothing approaches are compatible with the output data generated by these trained models and could be used to further reduce anomalous labels[32]. Moreover, systems that perform 3D pose estimation with multiple cameras can further reduce errors by identifying when a detection from one camera disagrees with the detections from the other cameras[32].

Together, these results demonstrate that large, diverse datasets are needed to train models capable of generalizing to different experimental setups, and that our fluorescence labeling approach can provide the necessary quality and quantity of training data.

2.5 Interactive optimization using live feedback

Even a deep learning model with good robustness can achieve higher accuracy when presented with input images that are more like the data it was trained on. Therefore, after a model is trained, another way to improve performance is to adjust the scene when collecting new video data to make the images captured by the cameras more suited to the preferred image properties of the model. We tested this optimization idea by designing a user interface for displaying the predictions of a deep learning model in real-time (**Supp. Fig. 4a**). The interface displays the most recent camera frame overlaid with the model's landmark prediction. It also displays a line plot of the *x*-position, *y*-position, and confidence of the most recent *k* landmark predictions (for our experiments, *k* was set to a value of 100).

To evaluate the usefulness of real-time feedback for increasing performance, we set up a camera to capture a head-fixed mouse performing a water reaching task (a behavioral setup not seen by the deep learning model during training). We collected a few seconds of video under three different conditions while monitoring model output. Between each video recording, the camera position and aperture settings were manually adjusted using real-time feedback to increase confidence and the stability of predictions. After video capture, we manually labeled these video frames for ground truth and evaluated model performance in each of the three clips (**Supp. Fig. 4b**). Performance improved in each of the successive camera adjustments, supporting the notion that optimizing a behavioral setup to suit a particular deep learning model using real-time kinematic and confidence value feedback is a feasible way to further improve performance during data collection.

2.6 Visual barcodes for massively parallel labeling

While the serial labeling pipeline can be repeated for each landmark we wish to track, this repetition becomes less practical if one wishes to track a large number of landmarks. To address this challenge, we adapted the fluorescence strategy to develop a parallel labeling approach that drastically increases the number of landmarks that can be labeled simultaneously. The fundamental idea is that local regions receive distinctive visual barcodes that can be tracked in parallel, yielding many landmark labels per frame instead of just one.

Using the human hand as proof-of-concept, we tested several methods for generating random visual barcodes: applying fluorescent powder suspended in transparent adhesive, applying liquid dye with an airbrush, and applying liquid dye by agitating the bristles of a brush to produce a fine aerosol. We found that the brush aerosol approach was most effective because of the scale and uniformity of the speckle pattern it produced (**Fig. 5a**). From the perspective of data collection, the only difference between serial and parallel labeling is the method by which the dye is applied: via aerosolization rather than with a marker. To validate our parallel labeling approach, we collected a video dataset containing 12,000 frames of a speckled hand captured at a rate of 10 image pairs per second, using the same dye, lighting, and cameras as above (though only the monochrome cameras were active). Finally, we captured 500 frames of video of an unlabeled hand with a different camera and lighting setup to be used as test data (the image scale was approximately 100 pixels per centimeter).

Visual barcodes are only useful for training deep learning models if they can be matched across images. For example, if the tip of the finger rotates in front of the camera as the hand moves, the barcodes from one frame need to be matched to the same barcodes in the other frames despite changes in orientation

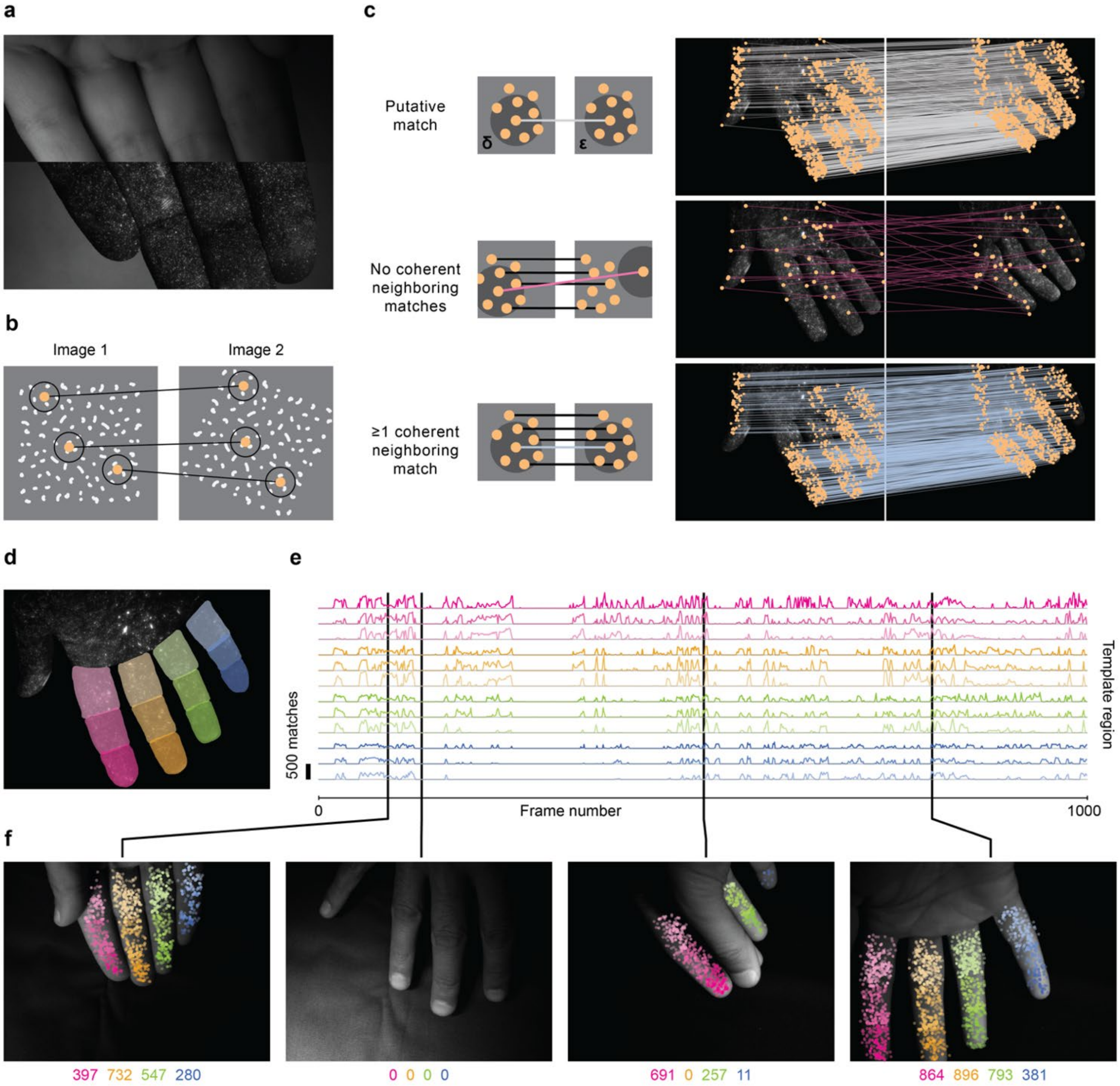

Fig. 5. Visual barcoding for massively parallel labeling. a) Adjacent frames of visible illumination (top) and UV illumination (bottom) of the hand with hidden fluorescent speckle pattern. **b)** Matching of visual barcodes between images using the SIFT algorithm. Each point represents a visual barcode, defined as a SIFT feature. The circle around each point represents the local image region from which the barcode descriptor is computed. **c)** A putative match (top left, gray line) between two barcodes in a pair of non-consecutive images. The dark disks around each barcode represent circles of radius δ and ε. All putative matches between barcodes in two images of the hand (top right). A putative match (middle left; pink line) with no coherent neighboring matches (black lines) is likely to be an incorrect match. All such matches between the two hand images (middle right), showing that these matches are nearly all spurious. A putative match (bottom left; light blue line) with at least one coherent neighboring match (black lines) is likely correct. All such matches between two hand images (bottom right). **d)** A template image with twelve manually labeled regions delineating 12 finger segments with the palm facing up. **e)** Twelve curves representing the number of SIFT matches between each video frame and the twelve finger segments (sum over ten labeled template images; see text). **f)** Four sample frames showing SIFT matches corresponding to the frame in **f.** Numbers indicate sum of SIFT matches on each digit (3 finger segments). When the palm is not visible (image 2) or a digit is occluded (image 3), no matches are detected.

and appearance. To address this challenge, we applied scale-invariant feature transform (SIFT)[33], a computer vision technique for matching distinctive key points (also known as features) between images (**Fig. 5b**). While other feature-matching algorithms that have been developed in recent years could also be used effectively, we selected the SIFT approach as it performs well on several quantitative benchmarks[34,35]. We found that matching SIFT features between pairs of UV images produced hundreds to thousands of matches, a small minority of them (typically <10%) being spurious (**Fig. 5c**).

To remove incorrect matches, we developed a spatial coherency heuristic as a filter. Considering a putative match, we defined a circle of radius δ around its left endpoint and a circle of radius ε around its right endpoint (**Fig. 5c**, top left**)**. For the match to be valid, it should have at least one coherent neighboring match: a match whose left endpoint is within the left circle and whose right endpoint is within the right circle. For the experiments shown here, we set δ and ε to 50 pixels. Visual inspection shows that most matches with no coherent neighboring matches are spurious (**Fig. 5c**, middle), and that the far more abundant matches with at least one coherent neighboring match are correct (**Fig. 5c**, bottom).

To visualize the number and accuracy of SIFT matches, we found it convenient to color code them according to which part of a template image they match. We accomplished this by manually labeling template images with an arbitrary number of different regions, in this case the twelve segments of the digits with the palm facing up (**Fig. 5d**). Denser SIFT coverage can be accomplished by selecting several template images, given the wide variety of configurations the hand can make. To identify an optimal set of template images (i.e., templates containing a diversity of poses with the 12 digit segments mostly visible), we devised a greedy algorithm that iteratively selects as a template the next image estimated to match with the greatest number of unmatched SIFT features (**Supp. Fig. 5**), which we then supplement with a small amount of human filtering. With this visualization approach, we find dense coverage of SIFT matches across all twelve digits, with essentially no spurious labels on the incorrect digit segment or when the segment is occluded (features pooled over 10 templates; 1000-frame clip) (**Fig. 5e,f** and **Supp. Video 4**). These results support the idea that thousands of fluorescent barcodes can effectively be matched across images. Moreover, only a small number of template frames (10 in this case) are needed to effectively cover the full 12,000-frame dataset, demonstrating the strong scaling properties of the approach.

In addition to using the fluorescent speckle pattern to produce labels, it can also be used to segment the object of interest from the background (**Supp. Fig. 6**). With accurate segmentation, the training set can be augmented by replacing the background with different random images. In our experiments, the random images were generated from a complex noise distribution, but they could alternatively be sampled from a set of natural images. This type of augmentation improves the accuracy and robustness of the resulting landmark detection models and was used for training the models reported below.

2.7 Using visual barcode matches to train deep learning models

Given a set of SIFT matches, additional processing is necessary to produce landmark labels that can be used as training data for deep learning models. For example, in a simple scheme we selected raw SIFT features from a template frame to act as landmarks. We then generated landmark labels for all other frames by simply matching the template SIFT features to the SIFT features in every other frame. Features that matched successfully received an (x, y) label, while those that did not were marked as absent. The downside to this scheme is that every failure in SIFT matching is translated directly into an erroneous training label. While SIFT matching with spatial coherency filtering produces very few false positives, there remain a problematic number of false negatives, as individual SIFT matches often drop out frame-to-frame. We found that deep learning models trained on landmarks derived directly from raw SIFT features failed to produce reasonable predictions (i.e., they had low correlation with ground truth positions), possibly indicating that training failed to converge to good model parameters due to the large number of erroneously missing labels. To address this issue and reduce labeling errors, we developed two schemes for pooling SIFT features together into local neighborhoods to provide resiliency to failed matches. The first scheme, which we call *manual neighborhood selection* (**Fig. 6a-f**), involves a modest amount of manual annotation; the second, which we call *automatic neighborhood selection* (**Fig. 6g-l**), is fully automated.

In *manual neighborhood selection*, the user selects a template image from the training set and manually draws a set of neighborhoods of interest over it, each representing a single landmark to track (**Fig. 6a,b**). The SIFT features within each segment then act as pooled template features for one landmark. These neighborhoods can be any size the user decides, but for proof-of concept we used the same digit segment templates used above for visualization (**Fig. 5d-f**). We then had these pooled features 'vote' on the location of the landmark in each training image by computing SIFT matches and then computing the centroid of all successful matches. In this way, the impact of false negatives is greatly reduced; as long as a few true positives are present, the centroid of the segment will be estimated accurately.

To further increase the reliability of matching, we labeled finger segments in not just one but ten template images, as described above (**Supp. Fig. 5**). We found that using more templates produced more matches, and that the greedy template selection algorithm resulted in 3 to 5 times as many SIFT matches as compared to random template sampling **(Fig. 6c)**. We then produced labeled training images with centroids overlaid onto the visible image of the hand across the image dataset **(Fig. 6d)**. For some images, no single template image was able to provide SIFT matches for all 12 segments, reinforcing the usefulness of using multiple optimized template images (**Supp. Fig. 7**).

We next used the labeled training data to train a network to identify our manually delineated landmarks (the 12 finger segments in this case) on unlabeled test data. To measure the impact of the

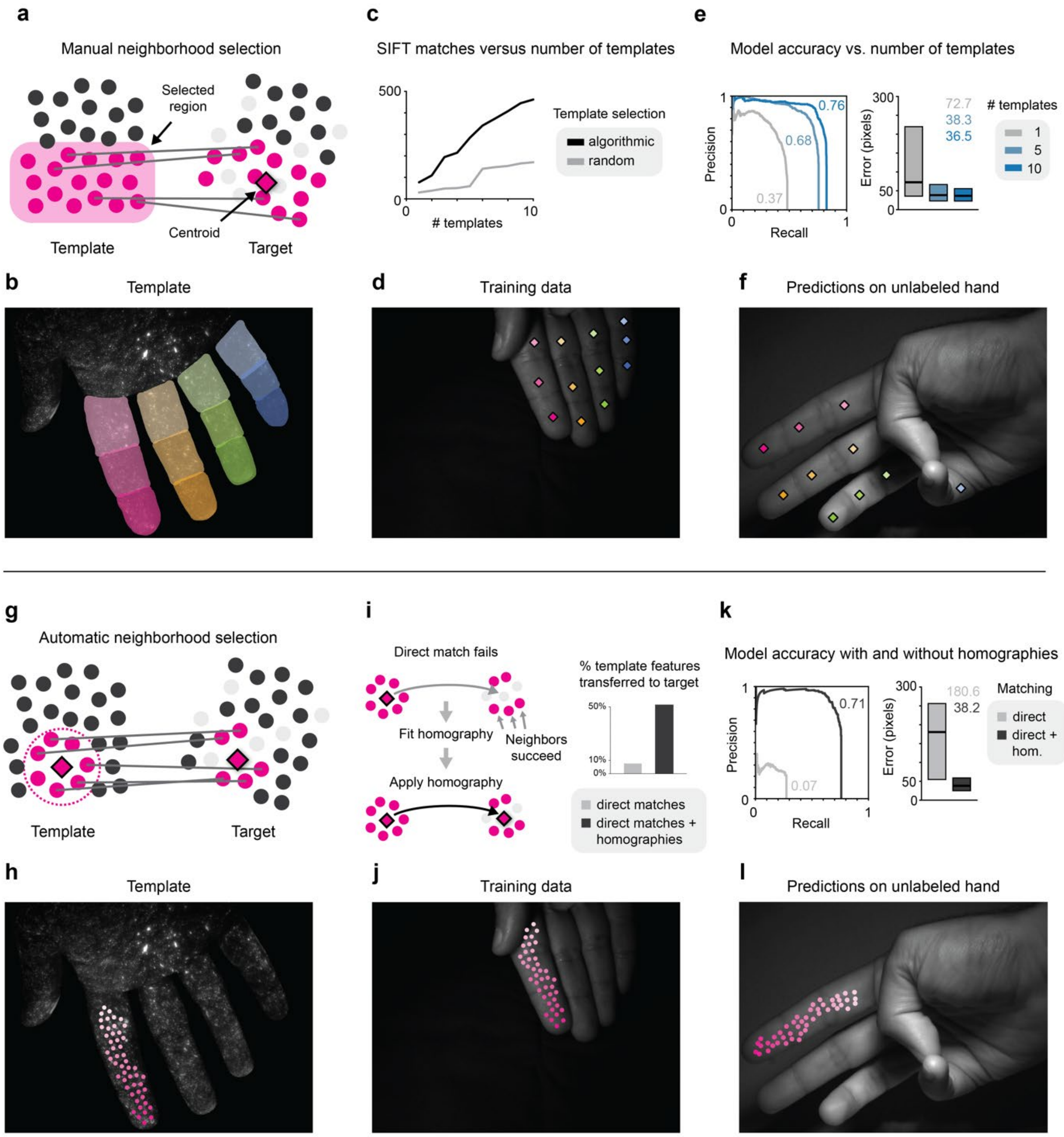

Fig. 6. **Pipelines for training landmark detectors from visual barcode data. a-f**) Manual neighborhood selection. **a)** A template image (left) is manually annotated with neighborhoods (light pink). SIFT features in the template image (pink circles) are matched to SIFT features in a target image (right). Successful matches from each template neighborhood are pooled to produce a single landmark label (centroid) in the target image (diamond). **b)** Example template image with 12 neighborhoods. **c)** Greedy algorithmic selection (black) produces more SIFT matches from a given number of template images compared to random selection (gray). SIFT matches increase with number of templates used (see **Supp. Fig. 5**). **d)** Example training image with labels derived from 10 annotated template images transferred to the visible light image. **e)** Precision-recall curves (left) and pixel error quartile plots (right) from testing on held-out data. Using more template images increases performance. **f)** Held-out evaluation image labeled by the trained model. Occluded regions do not receive a label. **g-l)** Automatic neighborhood selection. **g)** SIFT features are grouped by proximity to an active feature (left, diamond). **h)** A template image with features selected via spatially uniform subsampling on the first digit. The minimum distance between selected features is 30 pixels. **i)** If the active feature fails to match the target image, the neighborhood matches within a defined radius are used to estimate a local homography and reproject the active feature from template to target (left). The number of template features transferred to the target increases if homography is used. **j)** Example training image labeled using local homographies. **k)** Precision-recall curves (left) and pixel error quartile plots (right) from testing on held-out data. Using local homographies increases performance. **l)** Held-out evaluation image labeled by a model trained with homographies.

number of template images on end-to-end accuracy, we trained three deep learning models with labels generated from one, five, and ten template images. These models were evaluated on manually labeled images from a test set, and, as expected, the larger number of template images improved accuracy significantly (ten templates; AUC = 0.76; median pixel error = 36.5, one template; AUC = 0.37 median pixel error = 72.7) (**Fig. 6e,f** and **Supp. Video 5**).

Labeling the ten template images required about 30 minutes of labor. While this approach is feasible for a modest number of landmark neighborhoods (12 in this case), the amount of manual labor scales linearly with the number of landmarks and becomes more difficult with smaller neighborhoods that are harder to distinguish. We therefore sought to develop a fully automated method that could be scaled up to a practically arbitrary number and density of landmarks limited only by the underlying SIFT matches.

With *automatic neighborhood selection*, the local neighborhoods over which SIFT matches are pooled are circles of a user defined radius around each landmark feature (**Fig. 6g**). In this case, landmark features were selected on a single digit to be at least 30 pixels apart, giving relatively uniform coverage of the surface (**Fig. 6h**). Landmark labels were computed as follows: if a landmark feature matches a particular training image, then the match location is used as the landmark label. However, if a landmark feature fails to match but at least *k* other features in its local neighborhood match successfully, then the neighborhood matches are used to fit a local homography and project the template feature into the target image[36,37]; the projected location is then used as the landmark label (**Figure 6i**, left). The homography scheme greatly increases the percentage of landmark features that are successfully transferred to the target image, from less than 10% to over 50% (**Fig. 6i**, right; $k = 10$). Note that the maximum percentage is less than 100% because landmarks are absent in some frames. Training images with landmark labels were then generated across the entire dataset (**Fig. 6j**).

We next trained a deep learning model on 50 landmarks from a single digit generated with automatic neighborhood selection. Evaluation of network performance using automatically selected landmarks is challenging because of the large number of landmarks and because a human annotator cannot be given a simple description of each landmark to label as ground truth. We therefore evaluated the models against the manual labels of the digit segments used to evaluate manual neighborhood selection above. One landmark feature was selected as a proxy for each digit segment: specifically, the landmark feature that was closest to the ground truth label for that digit segment averaged over the entire evaluation set. We found that the use of homographies improved accuracy significantly when compared to a model trained on data labeled only from direct feature matches (AUC = 0.71 vs. 0.07; median pixel error = 38.2 vs. 180.6) (**Fig. 6k**). Using this approach, our model could reliably identify dozens of landmarks on an unlabeled hand (**Fig. 6k,l** and **Supp. Video 6**). More generally, these results show that rather than tracking a small number of visually identifiable points on a complex object like the hand, as is feasible with manual landmark annotation, one could approach dense coverage of the skin to monitor the contours and deformations as the object moves through space.

3 Discussion

We have described an approach for generating training datasets of sufficient size and diversity to create more versatile deep learning-based motion capture models. This large increase in volume and quality of training data is complementary to and can be combined with the many advances in training procedures and model architectures that are ongoing in the field of deep learning. Our methods can be used to label individual landmarks of interest serially, or massive numbers of landmarks in parallel. Together, the generalizability and scalability of these approaches enable automated pose detection and kinematic quantification across species with less effort, better accuracy, and higher resolution than is feasible with manual annotation approaches.

The field of markerless pose tracking for scientific applications has seen a surge of new methods as software tools and technical ideas from the human pose detection literature, particularly related to deep learning, have been adapted and optimized for new purposes[11-14,32,38,39]. Up to now the dominant paradigm for pose tracking in the laboratory has been to train new deep learning models for each experimental setup or dataset, but the field is increasingly moving towards more versatile, generalizable models that can be used in different settings without re-training. This trend is evident in several recent advances that, like ours, focus on synthesizing large-scale datasets. Within the realm of rodent pose tracking, notable approaches for generating labeled training data include: DANNCE[18], which uses a multi-camera setup and 3D reconstruction to propagate labels to many cameras; CAPTURE[19], which uses markers implanted in the skin; and work that uses a virtual 3D rodent to generate synthetic data[20]. For monkey pose tracking, OpenMonkeyStudio[40] developed a large training set using a many-camera setup and label propagation, while MacaquePose[41] labeled a large set of images of macaques in the wild. In the realm of human pose tracking, the HumanEva[5] and Human3.6M[42] pose datasets were created using marker-based motion capture, while the PoseStudio[43] dataset was created using a many-camera setup, 3D reconstruction, and label propagation. The recent FreiHand dataset[28] for human hand pose used a deformable 3D model to extract finger poses from multi-camera imagery.

Here, we take a different approach to generating large datasets for training pose estimation models – fluorescence labeling. Compared to other label generation techniques, fluorescence labeling has the advantage that it does not require a 3D model nor 3D reconstruction (which can pose challenges for some subjects). The approach is also simple in terms of computational requirements, making it an attractive option for many labs. Although this is conceptually a marker-based technique, fluorescent dye need only be applied to one or a small cohort of subjects to generate very large amounts of training data, and it may be tolerated better by laboratory animals than retroreflective markers or opaque paint. Some caveats to consider are that the dye must be compatible with the subject and the illumination intensity for dye excitation must be scaled up in proportion to the square of the distance to the subject.

There are several prior demonstrations of fluorescent imagery being used as a source of ground truth data for training predictive models. For instance, fluorescent labeling has recently been used to train deep learning models to predict features of interest in microscopy imagery[44,45]. Hidden fluorescent labels have also been used to generate ground truth data for computer vision, the most relevant for our approach being the Middlebury optical flow dataset[21]. In that work, several scenes were painted with a hidden fluorescent speckle pattern, and each scene was photographed under visible and UV illumination, both before and after a small perturbation to the scene. The speckle pattern visible in the UV images was used to compute the optical flow (i.e., the dense 2D correspondence map) between the images of the perturbed and unperturbed scenes, and ground truth data was used to optimize optical flow algorithms.

We extend the core idea of fluorescent labeling with several innovations: a) the use of fluorescent labels for training pose estimation models; b) the use of triphasic illumination for elimination of background fluorescence; c) the use of multiple light sources, camera types, camera angles, and behaviors to mitigate visual redundancy and increase diversity; and d) the use of visual barcodes and SIFT features to track and label many landmarks in parallel. While our work focuses on motion capture for life sciences research, the fluorescence labeling approaches we developed are general and could be used for other pose tracking applications in which objects of interest can be imaged offline, in a controlled setting, prior to model training.

The parallel labeling approach based on SIFT features offers a powerful way to densely track deformable surfaces like skin, but it still suffers from being limited to surfaces with certain properties. In particular, adapting parallel labeling to track many landmarks on the mouse still faces challenges with fur and is a goal of future work. Moreover, most commercially available fluorescent dyes decay too quickly to be used for our triphasic illumination scheme; we were only able to find one dye with the required millisecond-scale decay constant. Looking forward, the development of more dyes with millisecond-scale fluorescence lifetimes and a variety of emission wavelengths would enable a parallel fluorescence labeling approach based on color multiplexing that would combine some of the strengths of the serial and parallel labeling approaches presented here and would work well on a wider range of surface types, including on fur. Fluorescent and phosphorescent dyes for microscopy is one possible area relevant to developing more dyes with the desired properties[45-50].

With more versatile and automated pose estimation tools, behavioral research fields are generating rapidly growing amounts of movement data. Analytical techniques that can make sense of this type of motion data, several of which have already been developed[51-55], will continue to grow in usefulness. For example, techniques that can detect and characterize subtle changes in movement during early stages of disease could impact how prodromal pathology is detected and how therapeutic interventions are evaluated. Ultimately, these kinds of advances in tracking and quantifying movement can serve to support and augment the insights of well-trained human observers.

4 Methods

4.1 Hardware and software

Video capture was performed using eight USB3 cameras: four monochrome (Basler Ace acA1440-220um with 16mm Tamron lens M118FM16) and four color (Basler Ace acA1920-155uc with 8mm

Tamron lens M118FM08). The cameras were triggered by an Arduino Due microcontroller over GPIO output pins. Image capture was performed with a desktop computer using the Basler Pylon 5 C++ API.

UV illumination was provided by thirty LED modules (400-410nm; LED Supply, A008-UV400-65), each containing three LEDs, and mounted in five hexagonal clusters of six modules each. Each hexagonal cluster was constructed from a custom 3D-printed faceplate and backplate held together with machine screws, with the LED modules held in between. Visible illumination was provided by a similar LED configuration: five clusters containing four white LED modules each (LED Supply, CREEXHP35-765-3) and four clusters containing four red LED modules each (LED Supply, CREEXPE2-RED-3). LEDs were controlled by the same Arduino Due driving power MOSFETs, and power was supplied by a BK Precision 1672 variable power supply (Test Equipment Depot, 817050167207).

Cameras and LEDs were mounted to a 2V geodesic dome. The dome was constructed out of ¼-inch aluminum cylindrical struts with 3D-printed mounting attachments bonded to each end using a two-part epoxy (J-B Weld 50176 KwikWeld). Each vertex of the dome was a 3D-printed circular hub to which the struts were fastened with screws. This design allowed individual parts of the dome to be removed and re-arranged as needed by unfastening the appropriate screws. All 3D printing was performed with a FormLabs Form 2 using FormLabs Tough Resin (RS-F2-TOTL-05).

Inside the dome, the animal's behavioral apparatus was placed on a rotary turntable consisting of a ½-inch acrylic disk on a circular track. The acrylic disk was covered in a ¼-inch black urethane mat lightly sanded with medium grit sandpaper to increase friction.

The fluorescent dye used for the mouse and hand datasets was Opticz Bright Red UV Blacklight Reactive Invisible Ink (DirectGlow, DGINK1OZR).

4.2 Mouse *diverse* dataset collection

Data were obtained from adult C57BL/6 male and female mice (~8-12 weeks old) housed on a 12:12 hour light cycle. Procedures performed in this study were conducted according to US National Institutes of Health guidelines for animal research and were approved by the Institutional Animal Care and Use Committee of The Salk Institute for Biological Studies.

Prior to video capture, animals were anesthetized with 1-3% isoflurane and a felt-tipped marker was used to apply fluorescent dye to the target region. In all experiments reported, the entire hand, both ventral and dorsal, was coated in dye up to the wrist. The dye was allowed to dry for 5 minutes prior to video recording, and the animal was visually checked under UV illumination for stray dye outside of the target region.

Two animals were recorded performing three behaviors over two days: reaching, string pull, and free movement. The reaching task is described in detail elsewhere[8]. Briefly, the training protocol consisted of placing the mouse in a 20 cm tall × 8.5 cm wide × 19.5 cm long clear acrylic box with an opening in the end wall measuring 0.9 cm wide and 9 cm tall. A 3D-printed, 1.8 cm tall pedestal designed to hold a food pellet (20 mg, 3 mm diameter; Bio-Serv) was placed 1 cm away from the front of the box opening and displaced 0.5 cm lateral to the opening and opposite the preferred reaching forelimb. Food pellets were placed on top of the pedestal as the reaching target. Mice were food deprived to ~85% of their original bodyweight and trained to reach for food pellets for either 20 minutes or until 20 successful reaches (defined as pellet retrieval) were accomplished. The string pull behavior is described in detail elesewhere[56]. Briefly, animals were food deprived as described above. Ten to twenty strings were suspended above an open cage; one end of the string was placed within reach of the animal, and the other end was attached to a food reward. Animals quickly learned to pull the string into the cage to receive the reward. For the freely moving behavior, the animals did not receive any training or food rewards and were allowed to roam freely within the enclosure.

For all behaviors, cameras were triggered at a frame rate of 200 Hz and a resolution of 848x848 under alternating visible and UV illumination, and temporally adjacent frames were grouped into pairs. In both the biphasic and triphasic illumination schemes, the cameras and lights were triggered on a 10 ms cycle. For biphasic, UV illumination was on from 0 to 5 ms while visible illumination was on from 5 to 10 ms. Camera shutters were triggered at 2.5 ms and 7.5 ms, and the exposure duration was 2 ms. For triphasic, all time parameters were identical to biphasic with the exception that UV illumination was extinguished at 2.5 ms. For the freely moving behavior, to decrease data bandwidth, only 1 out of every 50 image pairs was recorded to disk (2 pairs per second). For the reaching and string pull behaviors, all image pairs were recorded at the full rate of 100 pairs per second, but to decrease data bandwidth, recording was only activated by the experimenter during individual reaches or string-pulling bouts. To decrease the number of frames missed due to the delay between behavior onset and the experimenter starting the video recording, image pairs were continuously saved to a 100-pair buffer in memory that was written to disk upon activation of video recording.

The *uniform* test set contained 1231 frames. The *diverse* test set contained 4438 test images, half of which were manually annotated with bounding boxes to compute the OKS-mAP metric (**Supp. Table 1**), and 600 of which were manually labeled with keypoint locations to compare fluorescence-derived labels with manual ground truth (**Supp. Fig. 3a**).

The diverse dataset and the training and testing subsets are publicly available for download (https://cnl.salk.edu/~dbutler/glowtrack).

4.3 Mouse *challenge* dataset collection

To create the *challenge* dataset, we sampled data from a variety of archival datasets. Represented in these datasets were mouse behavioral videos from two different labs (Azim and Goulding), six different behaviors (pellet reach, head-fixed water reach, treadmill, balance beam, open field, string pull), and both color and grayscale imagery. All data had been collected under different lighting conditions and from different cameras than the *diverse* dataset. The water reach, treadmill, string pull, and balance beam behaviors had been captured on behavioral apparatuses different from those represented in the *diverse* dataset.

Each archival dataset contained a different number of videos of different lengths. Simply combining all datasets would have resulted in a highly skewed number of frames per dataset. Therefore, we sampled 4-16 clips per dataset, depending on the specific video sizes, to achieve a more balanced number of frames from each dataset. From among those clips, we then sampled 660 random images to receive ground truth labels.

To produce ground truth labels for the *challenge* set, we manually labeled the sampled images using LabelStudio[57], an open-source web application. Each frame was labeled by two annotators. Annotators were instructed not to guess the location of any landmark unless it was obvious. If a landmark was out of the camera's field of view or occluded such that it was impossible to know its precise location, then the annotator was instructed to record that landmark as absent. Only frames for which both annotators marked the landmark as absent or the annotators' labels were within 5 pixels of each other were retained in the final label set. The two annotators' landmark locations for each frame were averaged to produce the final ground truth location. After the label reconciliation process, there were 612 labeled images in the *challenge* set.

4.4 Deep learning model training

The deep learning model used for all experiments was the DeeperCut model, which is based on the ResNet-101 architecture pre-trained on ImageNet and fine-tuned on the given training dataset[10,30,58]. We trained each model for 4.12 million training iterations with an image pre-scaling factor of 0.8. These parameter values were each selected using 1-D grid search. All other training parameters were set to their default values. During training we performed more extensive data augmentation than the original DeeperCut implementation. Prior to each training image being consumed by DeeperCut, it was randomly perturbed using the "imgaug" Python package. To each training image we randomly applied Gaussian blur (sigma between 0.0 and 0.5), random contrast scaling (scale factor between 0.75 and 1.5), additive Gaussian noise (sigma of 5% maximum intensity), random channel scaling (scale factor between 0.8 and 1.2), random cropping (0-10%), random affine warping (scale 0.8-1.2, translation 0.8-1.2, rotation +/- 15 degrees, sheer +/- 8 degrees), and conversion of color images to grayscale with 50% probability.

For the human hand dataset, we computed a fluorescence mask to segment the hand from the background and augmented the training data with random synthetic background imagery. The random background was generated via the composition of several noise functions producing both high and low spatial frequency noise.

4.5 Label post-processing and real-time optimization

Scale optimization was performed at test time using 1-D hierarchical grid search with two levels. First, the objective was computed over a coarse range of scales (2^k for k ranging from -1 to 1 in increments of 0.5), and then over a finer range of scales centered on the optimal value from the previous level (2^{k+j} for j ranging from -0.33 to 0.33 in increments of 0.16). We experimented with two proxy metrics:

smoothness, as measured by the average landmark displacement distance between adjacent frames (i.e., average speed); and confidence, as defined by the average confidence of the model's predictions over the entire clip. We found that occasionally the smoothness metric failed to capture the accuracy of the trajectory; sometimes highly smooth trajectories were nevertheless spurious. The confidence metric did not appear to suffer from this type of failure. Therefore, all experiments presented were performed using mean confidence as the objective function being optimized. For image-level scale optimization, this search procedure was repeated independently for each image. For clip-level scale optimization, the procedure was performed once for all images in a video.

To enable real-time visualization for interactive adjustment of image capture, we developed a user interface in which the live video is displayed to the user with the model's predicted landmark label overlaid, alongside a plot of the landmark's most recent 100 x positions, y positions, and confidence values over time. The plot is continuously updated in real-time, allowing the user to adjust the position of the animal, camera, and lighting interactively.

4.6 Visual barcoding

Dye was applied to the human hand using a brush to aerosolize it into a fine mist: a stiff toothbrush was loaded with dye, the bristles were agitated, and the resulting mist was allowed to settle on the target object. This procedure was conducted under UV illumination to monitor coverage of the target, and the dye was allowed to dry for five minutes.

Video data were collected using the same video capture setup described above from one hand. OpenCV[37] was used to compute SIFT features and perform SIFT matching. SIFT features were computed with a contrast threshold of 0.01, and all other parameters were set to their default values.

To reduce the number of spurious matches, we performed spatial coherency filtering. In our filtering algorithm, for a putative match (*a*, *b*) to be considered valid, it must have at least one coherent neighboring match. A neighboring match (*c*, *d*) is considered coherent if the left endpoints *a* and *c* are within a distance of δ and *b* and *d* are within a distance of ε. We set δ and ε equal to 50 pixels for our experiments. Neighboring matches were computed efficiently using the KD tree implantation from the "scipy.spatial" Python package[59].

When selecting template atlas images, an algorithm was used to rank all training images. Our ranking algorithm is iterative and greedy; it repeatedly selects the next best image from the training set. Specifically, it selects the training image that matches the greatest number of unmatched SIFT features in the training set. Then, all SIFT features that the selected image matches are marked as having been matched. We implemented the algorithm by modifying published C++ code[60] to perform large-scale approximate SIFT matching using a vocabulary tree[61]. Specifically, we changed the vocabulary tree implementation so as to compute the simple weighting scheme described above rather than the more complex TFIDF scheme from the original paper[61].

First, SIFT features are computed for all images in the training set and grouped into 500,000 clusters using an approximate k-means algorithm. Each feature is assigned a weight equal to the number of features in its cluster. Then, each image is assigned a weight equal to the sum of the weights of its features; the image weight represents an estimate of the number of features across the entire dataset that would be matched by that image. The image with the greatest weight is the next image selected by the algorithm. Finally, the weights of features matched by the selected image are decremented, all image weights are updated, and the next image is selected. We automatically selected the top 100 template candidates using this procedure, and manually refined the list down to 10 final template images covering the palm of the hand. We then used Adobe Photoshop to create 12 binary masks for each template image, indicating the extent of the 12 finger segments in that template.

To visualize and quantify the number of SIFT matches, we started with a video clip of length 1000 frames containing no template images. We computed the number of matches between each template image and each frame of the clip. Then for each finger segment, we computed the total number of matches across all templates. This procedure resulted in 12 numbers representing match counts for each finger segment in each frame of the clip. Finally for each frame, we overlaid a scatter plot with the matches from each template segment in a different color.

The manual neighborhood selection pipeline for generating labels is very similar to the process described above. The only difference is an additional step in which all matches corresponding to a segment are pooled together to produce a label for that segment. Pooling was performed in the following way: if the segment had at least 5 matches, then the median of the x-values and y-values were used as the x and y position of the label, respectively. If the segment had fewer than 5 matches, it was recorded as absent. Labels produced in this way were then used to train a DeeperCut model to predict the location of the 12 finger segments. For evaluation, ground truth labels were generated manually with LabelStudio.

The automatic neighborhood selection pipeline is structured as follows. First, a single template image was selected as the base image. A subset of SIFT features in the base image were selected by iteratively selecting one SIFT feature and then removing all other features within 30 pixels (using a KD tree), resulting in a set of template features with a minimum spacing of 30 pixels. These template features form the set of landmarks tracked by the deep learning model. For each video frame in the training set, SIFT matches were computed between the base image and the target frame. For template features that matched the target image, the position of the match in the target image was used as the landmark position. If a particular template feature failed to match the target, then neighboring features within a radius of 30 pixels that had successfully matched were used as proxies; those feature matches were used to fit a local homography using OpenCV[37]. That homography was then used to transform the position of the original template feature from the base image into the target image.

Data Availability

Materials available on a publicly available Github repository (https://github.com/azimlabsalk/glowtrack) include: design files for dome fabrication; image capture code; Arduino control code; software packages for processing strobed fluorescence video, generating motion capture models, and evaluating model performance; and a GUI for real-time viewing of strobed fluorescence video and motion capture model output. The main image datasets that support the findings of this study are publicly available online (https://cnl.salk.edu/~dbutler/glowtrack) and upon request.

Acknowledgements

We are grateful to E. Sanders, A. Thanawalla, and N. Baltar (Salk Institute) for providing trained mice and archival video datasets; G. Gatto (Salk Institute, Uniklinik Köln), Martyn Goulding (Salk Institute), and K.W. Huang (Salk Institute) for providing archival video data; P. Nguyen (Salk Institute) for assistance with mouse husbandry and lab operations; A. Aeruva, N. Benhaim, H. Gao, J. Khatibi, M. Ochoa, P. Nguyen, D. Saklaway, and G. Salmun (Salk Institute) for labeling images; N. Baltar (Salk Institute) for assistance with building the dome; K. Cortes (Salk Institute) for data collection; and B. Brunton, P. Karashchuk, U. Manor, T. Pereira, J. Tuthill and members of the Azim lab for valuable discussion and comments on the manuscript. A.P.K. was supported by the UCSD CMG Training Program and a Jesse and Caryl Philips Foundation Award; E.A. was supported by the National Institutes of Health

(R00NS088193, DP2NS105555, R01NS111479, and U19NS112959), a Salk Institute Innovation Grant, the Searle Scholars Program, The Pew Charitable Trusts, and the McKnight Foundation.

Author Contributions

Conceptualization and design: D.J.B., E.A.; Data collection: D.J.B., A.P.K.; Hardware development: D.J.B., A.P.K.; Software development: D.J.B.; Algorithm evaluation: D.J.B., S.R.; Data analysis: D.J.B.; Manuscript preparation: D.J.B., E.A.

Competing interests

The authors declare no competing interests.

Supplementary Information

Supplementary Information is available for this paper.

Correspondence

Correspondence and requests for data and code should be addressed to E.A. (eazim@salk.edu).

References

1 Tinbergen, N. On aims and methods of Ethology. *Zeitschrift für Tierpsychologie* **20**, 410-433, doi:https://doi.org/10.1111/j.1439-0310.1963.tb01161.x (1963).

2 Whishaw, I. Q. & Pellis, S. M. The structure of skilled forelimb reaching in the rat: A proximally driven movement with a single distal rotatory component. *Behavioural Brain Research* **41**, 49-59 (1990).

3 Chan, S. S. & Moran, D. W. Computational model of a primate arm: from hand position to joint angles, joint torques and muscle forces. *Journal of neural engineering* **3**, 327 (2006).

4 Peikon, I. D., Fitzsimmons, N. A., Lebedev, M. A. & Nicolelis, M. A. Three-dimensional, automated, real-time video system for tracking limb motion in brain–machine interface studies. *Journal of neuroscience methods* **180**, 224-233 (2009).

5 Sigal, L., Balan, A. O. & Black, M. J. HumanEva: Synchronized Video and Motion Capture Dataset and Baseline Algorithm for Evaluation of Articulated Human†Motion. *International Journal of Computer Vision* **87**, 4-27 (2009).

6 Fitzsimmons, N., Lebedev, M., Peikon, I. & Nicolelis, M. A. Extracting kinematic parameters for monkey bipedal walking from cortical neuronal ensemble activity. *Frontiers in integrative neuroscience* **3**, 3 (2009).

7 Vargas-Irwin, C. E. *et al.* Decoding complete reach and grasp actions from local primary motor cortex populations. *Journal of neuroscience* **30**, 9659-9669 (2010).

8 Azim, E., Jiang, J., Alstermark, B. & Jessell, T. M. Skilled reaching relies on a V2a propriospinal internal copy circuit. *Nature* **508**, 357 - 363 (2014).

9 LeCun, Y., Bottou, L., Bengio, Y. & Haffner, P. Gradient-based learning applied to document recognition. *Proceedings of the IEEE* **86**, 2278-2324 (1998).

10 Goodfellow, I., Bengio, Y. & Courville, A. *Deep learning*. (MIT press, 2016).

11 Mathis, A. *et al.* DeepLabCut: markerless pose estimation of user-defined body parts with deep learning. *Nature Neuroscience* **21**, 1281-1289 (2018).

12 Pereira, T. D. *et al.* Fast animal pose estimation using deep neural networks. *Nature Methods* **16**, 117-125, doi:10.1038/s41592-018-0234-5 (2019).

13 Pereira, T. D. *et al.* SLEAP: Multi-animal pose tracking. *bioRxiv* (2020).

14 Graving, J. M. *et al.* DeepPoseKit, a software toolkit for fast and robust animal pose estimation using deep learning. *Elife* **8**, e47994, doi:10.7554/eLife.47994 (2019).

15 Machado, A. S., Darmohray, D. M., Fayad, J. o., Marques, H. G. & Carey, M. R. A quantitative framework for whole-body coordination reveals specific deficits in freely walking ataxic mice. *Elife* **4** (2015).

16 Mathis, A., Schneider, S., Lauer, J. & Mathis, M. W. A Primer on Motion Capture with Deep Learning: Principles, Pitfalls, and Perspectives. *Neuron* **108**, 44-65, doi:10.1016/j.neuron.2020.09.017 (2020).

17 Hausmann, S. B., Vargas, A. M., Mathis, A. & Mathis, M. W. Measuring and modeling the motor system with machine learning. *Curr Opin Neurobiol* **70**, 11-23, doi:10.1016/j.conb.2021.04.004 (2021).

18 Dunn, T. W. *et al.* Geometric deep learning enables 3D kinematic profiling across species and environments. *Nature Methods* **18**, 564-573 (2021).

19 Marshall, J. D. *et al.* Continuous Whole-Body 3D Kinematic Recordings across the Rodent Behavioral Repertoire. *Neuron* **109**, 420-437.e428 (2021).

20 Bolaños, L. A. *et al.* A 3D virtual mouse generates synthetic training data for behavioral analysis. *Nature methods* **18**, 378 - 381 (2021).

21 Baker, S. *et al.* A Database and Evaluation Methodology for Optical Flow. *International Journal of Computer Vision* **92**, 1-31 (2007).

22 Klein, A. M. *et al.* Droplet Barcoding for Single-Cell Transcriptomics Applied to Embryonic Stem Cells. *Cell* **161**, 1187-1201 (2015).

23 Zilionis, R. *et al.* Single-cell barcoding and sequencing using droplet microfluidics. *Nature Protocols* **12**, 44-73 (2017).

24 Macosko, E. Z. *et al.* Highly Parallel Genome-wide Expression Profiling of Individual Cells Using Nanoliter Droplets. *Cell* **161**, 1202-1214 (2015).

25 Ballan, L., Taneja, A., Gall, J., Gool, L. V. & Pollefeys, M. Motion Capture of Hands in Action Using Discriminative Salient Points. *European Conference on Computer Vision* (2012).

26 Mueller, F. *et al.* GANerated Hands for Real-Time 3D Hand Tracking from Monocular RGB. *2018 IEEE/CVF Conference on Computer Vision and Pattern Recognition*, 49-59 (2018).

27 Oikonomidis, I., Kyriazis, N. & Argyros, A. A. Efficient model-based 3D tracking of hand articulations using Kinect. *British Machine Vision Conference* (2011).

28 Zimmermann, C. *et al.* FreiHAND: A Dataset for Markerless Capture of Hand Pose and Shape From Single RGB Images. *2019 IEEE/CVF International Conference on Computer Vision (ICCV)*, 813-822 (2019).

29 Walt, S. v. d. *et al.* scikit-image: image processing in Python. *PeerJ* **2** (2014).

30 Insafutdinov, E., Pishchulin, L., Andres, B., Andriluka, M. & Schiele, B. in *ECCV.*

31 Ronchi, M. R. & Perona, P. Benchmarking and Error Diagnosis in Multi-instance Pose Estimation. *2017 IEEE International Conference on Computer Vision (ICCV)*, 369-378 (2017).

32 Karashchuk, P. *et al.* Anipose: A toolkit for robust markerless 3D pose estimation. *Cell reports* **36 13**, 109730 (2021).

33 Lowe, D. G. Distinctive Image Features from Scale-Invariant Keypoints. *International Journal of Computer Vision* **60**, 91-110 (2004).

34 Jin, Y. *et al.* Image Matching Across Wide Baselines: From Paper to Practice. *International Journal of Computer Vision* **129**, 517-547 (2021).

35 Schönberger, J. L., Hardmeier, H., Sattler, T. & Pollefeys, M. Comparative Evaluation of Hand-Crafted and Learned Local Features. *2017 IEEE Conference on Computer Vision and Pattern Recognition (CVPR)*, 6959-6968 (2017).

36 Szeliski, R. *Computer vision: algorithms and applications*. (Springer Science & Business Media, 2010).

37 Bradski, G. & Kaehler, A. OpenCV. *Dr. Dobb's journal of software tools* **3** (2000).

38 Lauer, J. *et al.* Multi-animal pose estimation and tracking with DeepLabCut. *bioRxiv* (2021).

39 Zuffi, S., Kanazawa, A., Jacobs, D. W. & Black, M. J. 3D Menagerie: Modeling the 3D Shape and Pose of Animals. *2017 IEEE Conference on Computer Vision and Pattern Recognition (CVPR)*, 5524-5532 (2017).

40 Bala, P. C. *et al.* Automated markerless pose estimation in freely moving macaques with OpenMonkeyStudio. *Nature Communications* **11** (2020).

41 Labuguen, R. T. *et al.* MacaquePose: A novel in the wild macaque monkey pose dataset for markerless motion capture. *bioRxiv* (2020).

42 Ionescu, C., Papava, D., Olaru, V. & Sminchisescu, C. Human3.6M: Large Scale Datasets and Predictive Methods for 3D Human Sensing in Natural Environments. *IEEE Transactions on Pattern Analysis and Machine Intelligence* **36**, 1325-1339 (2014).

43 Joo, H. *et al.* Panoptic Studio: A Massively Multiview System for Social Motion Capture. *2015 IEEE International Conference on Computer Vision (ICCV)*, 3334-3342 (2015).

44 Christiansen, E. M. *et al.* In Silico Labeling: Predicting Fluorescent Labels in Unlabeled Images. *Cell* **173**, 792-803.e719 (2018).

45 Wang, H. *et al.* Deep learning enables cross-modality super-resolution in fluorescence microscopy. *Nature Methods* **16**, 103-110 (2018).

46 Lakowicz, J. R. *Principles of fluorescence spectroscopy*. (Springer, 2006).

47 Li, D. D.-U. *et al.* Video-rate fluorescence lifetime imaging camera with CMOS single-photon avalanche diode arrays and high-speed imaging algorithm. *Journal of biomedical optics* **16 9**, 096012 (2011).

48 Poudel, C., Mela, I. & Kaminski, C. F. High-throughput, multi-parametric, and correlative fluorescence lifetime imaging. *Methods and Applications in Fluorescence* **8** (2020).

49 Howard, S. S., Straub, A., Horton, N. G., Kobat, D. & Xu, C. Frequency Multiplexed In Vivo Multiphoton Phosphorescence Lifetime Microscopy. *Nature photonics* **7**, 33 - 37 (2013).

50 Vanderkooi, J. M., Maniara, G., Green, T. J. & Wilson, D. F. An optical method for measurement of dioxygen concentration based upon quenching of phosphorescence. *The Journal of biological chemistry* **262 12**, 5476-5482 (1987).

51 Branson, K., Robie, A., Bender, J. A., Perona, P. & Dickinson, M. H. High-throughput Ethomics in Large Groups of Drosophila. *Nature methods* **6**, 451 - 457 (2009).

52 Wiltschko, A. B. *et al.* Mapping Sub-Second Structure in Mouse Behavior. *Neuron* **88**, 1121-1135 (2015).

53 Berman, G. J., Bialek, W. & Shaevitz, J. W. Predictability and hierarchy in Drosophila behavior. *Proceedings of the National Academy of Sciences* **113**, 11943 - 11948 (2016).

54 Calhoun, A. J., Pillow, J. W. & Murthy, M. Unsupervised identification of the internal states that shape natural behavior. *Nature Neuroscience* **22**, 2040 - 2049 (2019).

55 Dennis, E. J. *et al.* Systems Neuroscience of Natural Behaviors in Rodents. *The Journal of Neuroscience* **41**, 911 - 919 (2021).

56 Conner, J. M. *et al.* Modulation of tactile feedback for the execution of dexterous movement. *Science* **374**, 316-323 (2021).

57 Tkachenko, M., Malyuk, M., Shevchenko, N., Holmanyuk, A. & Liubimov, N. *Label Studio: Data labeling software*, <http://github.com/heartexlabs/label-studio> (2021).

58 He, K., Zhang, X., Ren, S. & Sun, J. Deep Residual Learning for Image Recognition. *2016 IEEE Conference on Computer Vision and Pattern Recognition (CVPR)*, 770-778 (2016).

59 Virtanen, P. *et al.* SciPy 1.0: fundamental algorithms for scientific computing in Python. *Nature Methods* **17**, 261 - 272 (2020).

60 Agarwal, S., Snavely, N., Simon, I., Seitz, S. M. & Szeliski, R. in *ICCV*.

61 Nistér, D. & Stewénius, H. Scalable Recognition with a Vocabulary Tree. *2006 IEEE Computer Society Conference on Computer Vision and Pattern Recognition (CVPR'06)* **2**, 2161-2168 (2006).

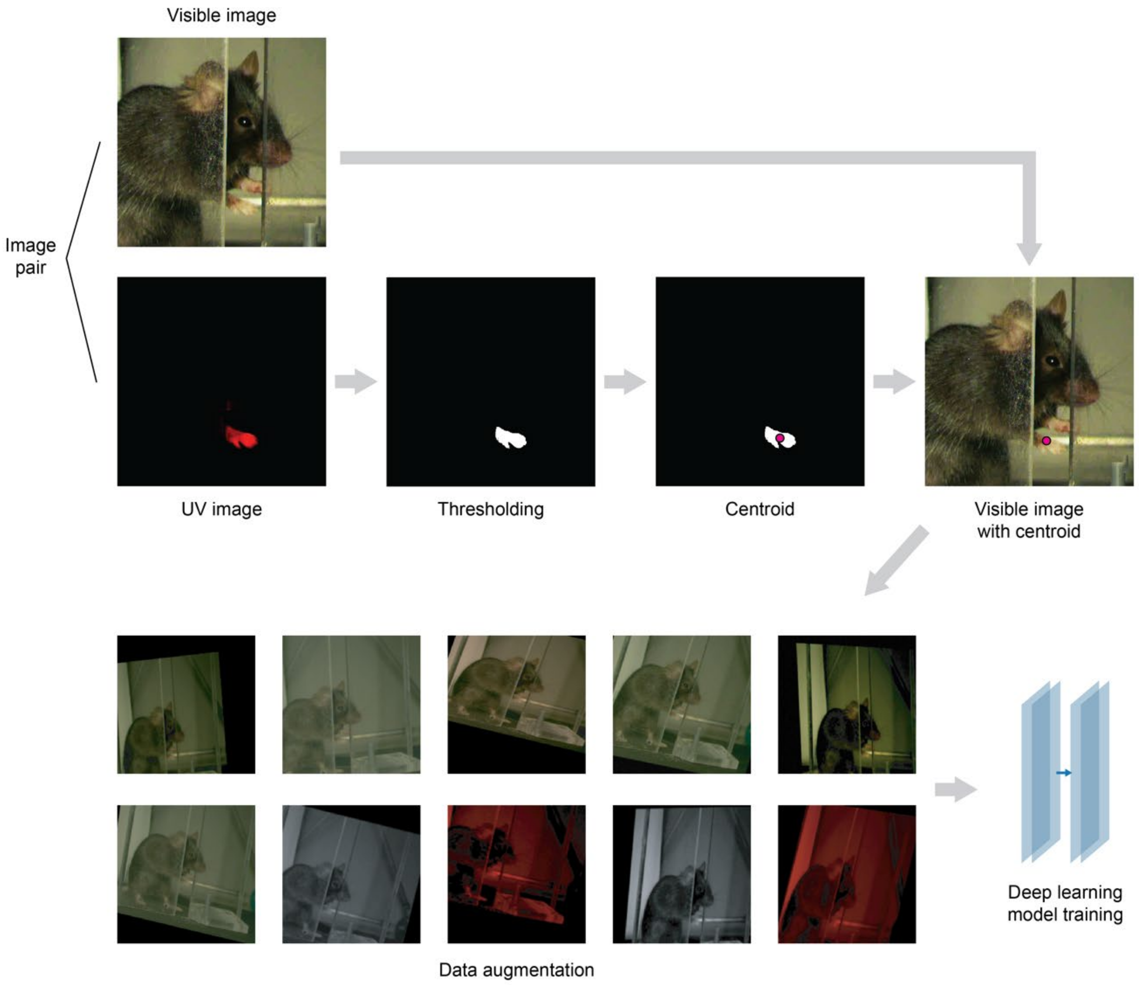

Supp. Fig. 1. **Conversion of raw imagery into labeled training data.** The data processing pipeline for a visible image (top left) and its corresponding UV image. The UV image is first thresholded to produce a dye mask, and the centroid of the dye mask is computed. The centroid is used as a proxy label for the subsequent visible image. During training, each labeled training image is augmented with scaling, rotating, shear, Gaussian noise, and random scaling of hue. In addition, the image is converted to grayscale or the non-red channels are set to zero, both with a fixed probability, to simulate monochrome imagery and red illumination, respectively (see Methods). Example augmented images are shown.

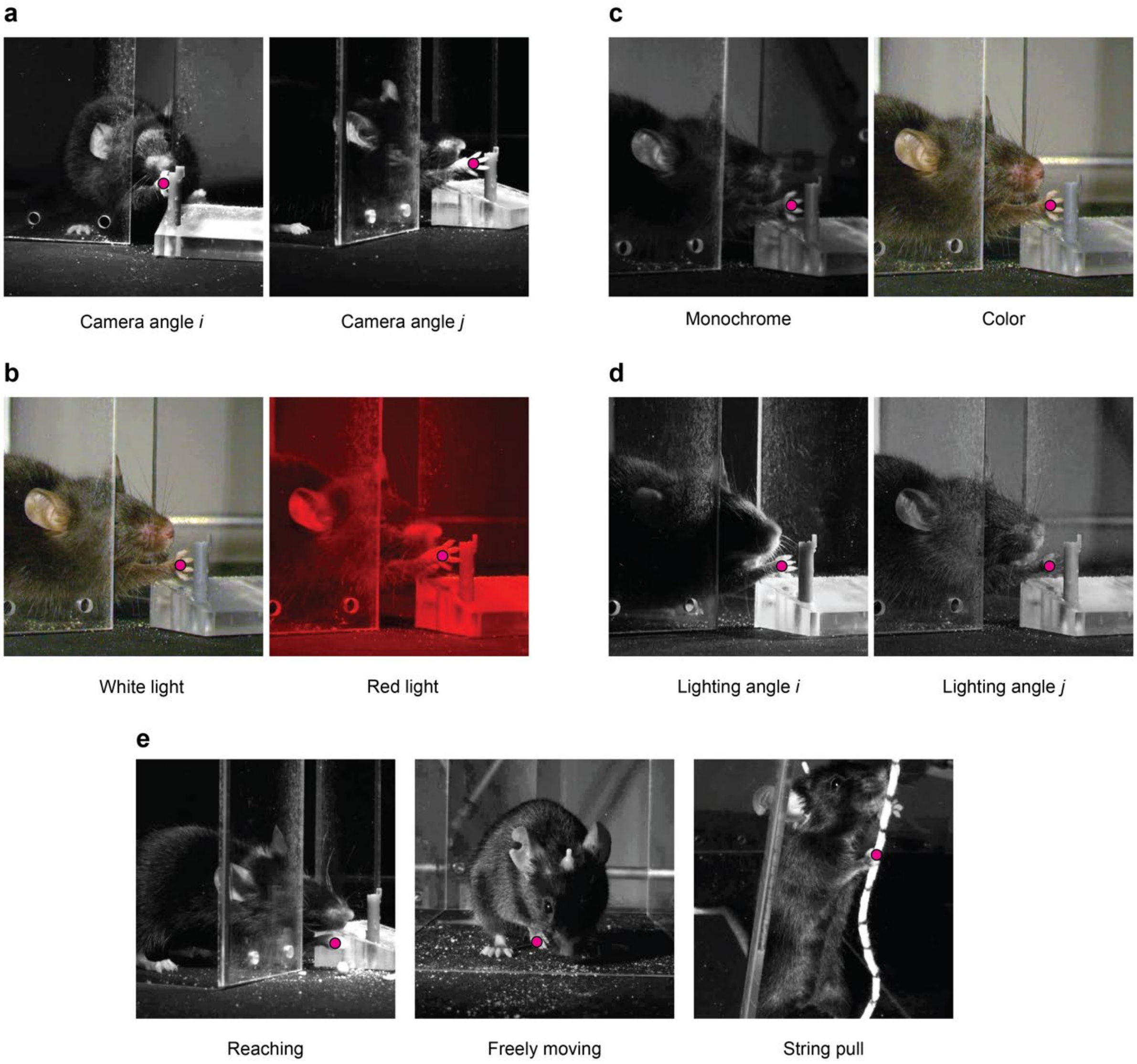

Supp. Fig. 2. Image diversity in the fluorescence-derived mouse dataset. Images captured: **a)** simultaneously from two cameras; **b)** sequentially under white and red illumination; **c)** simultaneously from monochrome and color cameras; **d)** under different lighting angles; and **e**) during reaching behavior (left), freely moving behavior (middle), and string pull behavior (right). Landmark labels (magenta dots) are derived from the corresponding fluorescence images (not shown). Panels **a** and **b** are reproduced from **Fig. 3**.

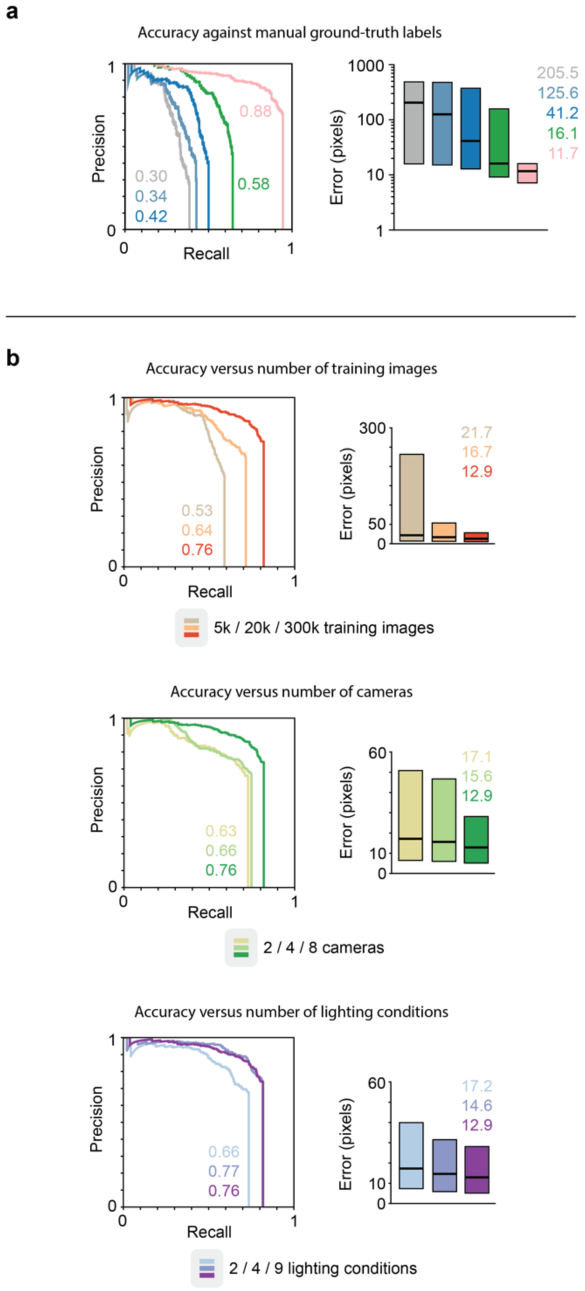

Supp. Fig. 3. Contributions of ground truth source and training set parameters to neural network performance. Precision-recall curves (left) and pixel error quartile plots (right). **a)** Results on the *diverse* test set, but with manual rather than fluorescence-derived ground truth labels. Values are similar to those produced when evaluating against fluorescence-derived labels (compare to **Fig. 3h**), confirming that fluorescence-derived labels are a valid source of ground truth. **b)** Results on the *challenge* data set for neural networks trained on different subsets of the fluorescence-derived training set. The number of cameras, the number of lighting conditions, and the number of training images all contribute to AUC and median pixel error.

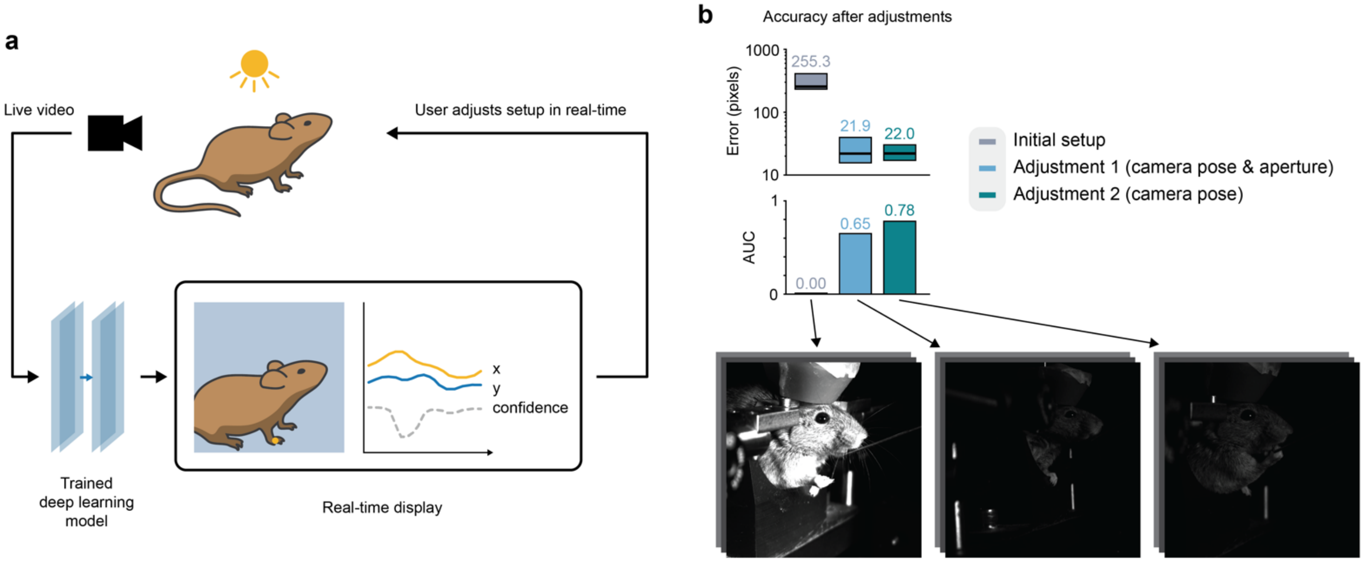

Supp. Fig. 4. Real-time visualization enables interactive adjustment and improved performance. a) A live video stream is captured and processed by a trained deep learning model that predicts landmark position. The live video is displayed to the user with the predicted landmark label overlaid and a plot of its most recent 100 x positions, y positions, and confidence values over time. The plot is continuously updated in real-time, allowing the user to adjust the position of the animal, camera, and lighting interactively while visualizing the impact on the model's predictions. **b)** Pixel error quartiles (top) and AUC values (middle) for three different positions of the camera and settings of the camera lens aperture. Sample images from each setup are shown at bottom. Performance increases over time as the user makes adjustments to the setup to produce images that are better suited to the trained model.

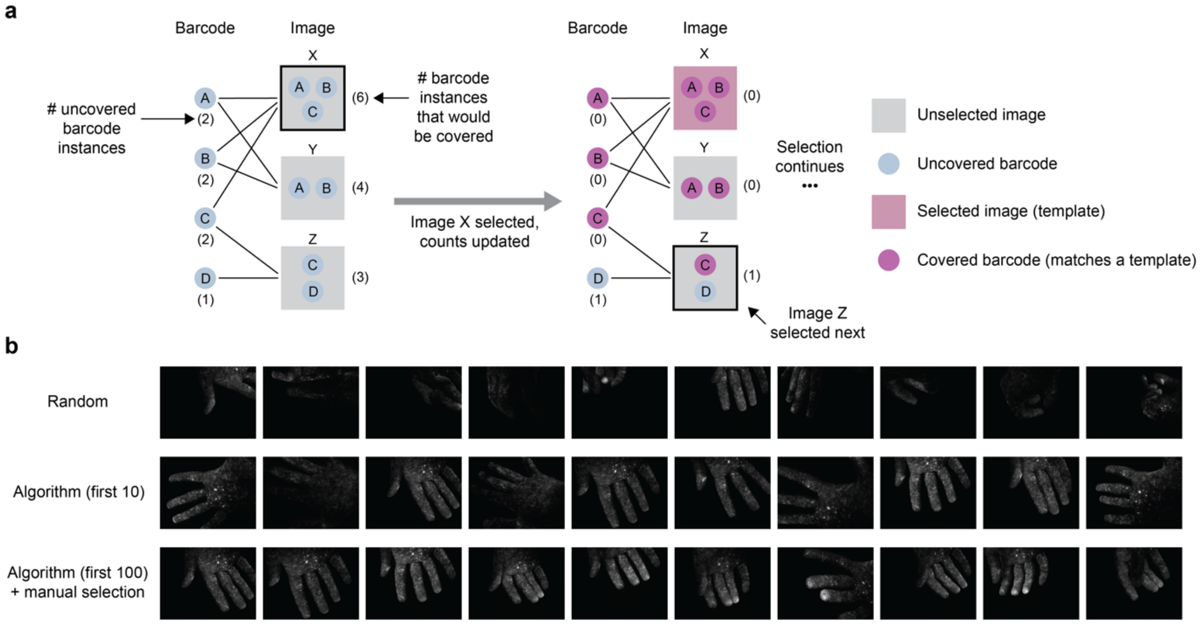

Supp. Fig. 5. Greedy algorithm for template image selection. a) An estimate of the number of barcode instances that would be matched (covered) by each candidate template image is calculated (left). The image with the highest instance coverage (black outline) is selected as the next template image, the counts are updated (right), and the procedure is repeated until the desired number of template images have been selected. **b)** Examples of 10 template images selected randomly (top) and by the greedy algorithm (middle). To train a network that labels landmarks on the palm side of the hand, images that depict that specific region (bottom) were manually selected from among the top 100 images as ranked by the greedy algorithm.

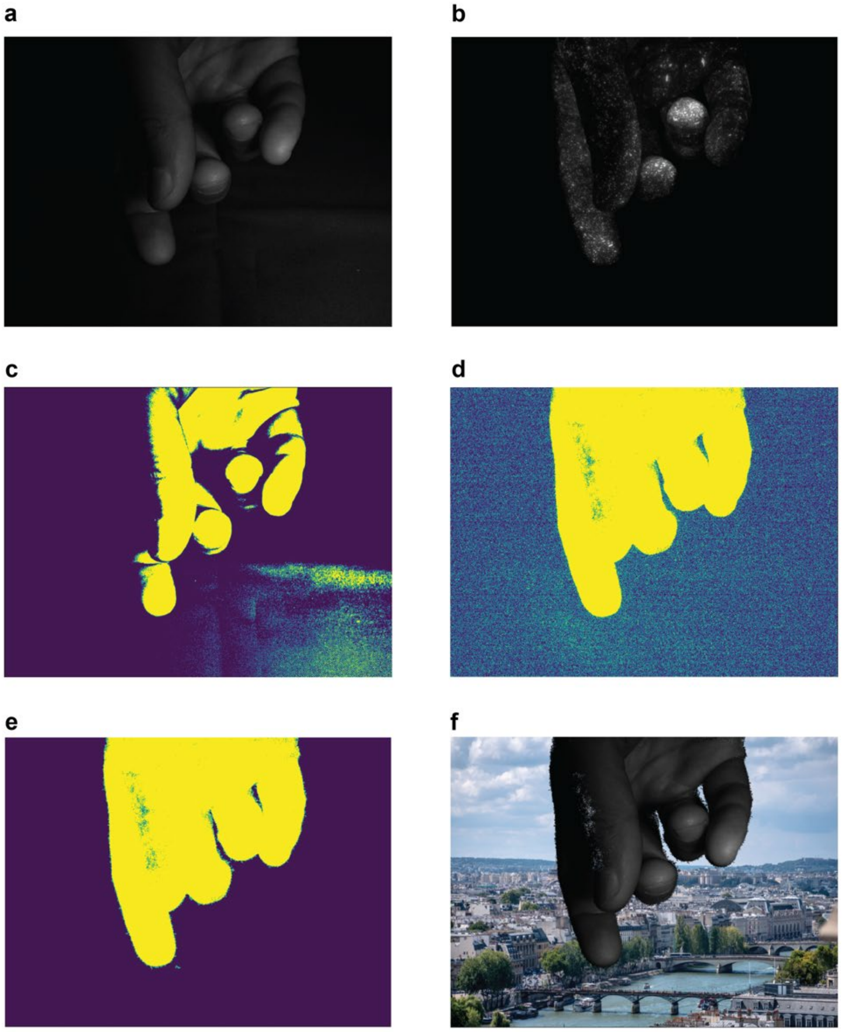

Supp. Fig. 6. **Background segmentation and augmentation using fluorescence. a)** Visible image; **b)** UV image; **c)** thresholded visible image, which does not provide a clean foreground mask due to shadows; **d)** thresholded UV image, which provides a cleaner foreground mask; **e)** thresholded UV image with morphological erosion to reduce spurious background signal (see Methods); **f)** target object segmented and superimposed onto a synthetic background image, using image from panel **e** as mask. During training, the image background is augmented to increase the model's robustness to any changes in the scene that happen away from the target object.

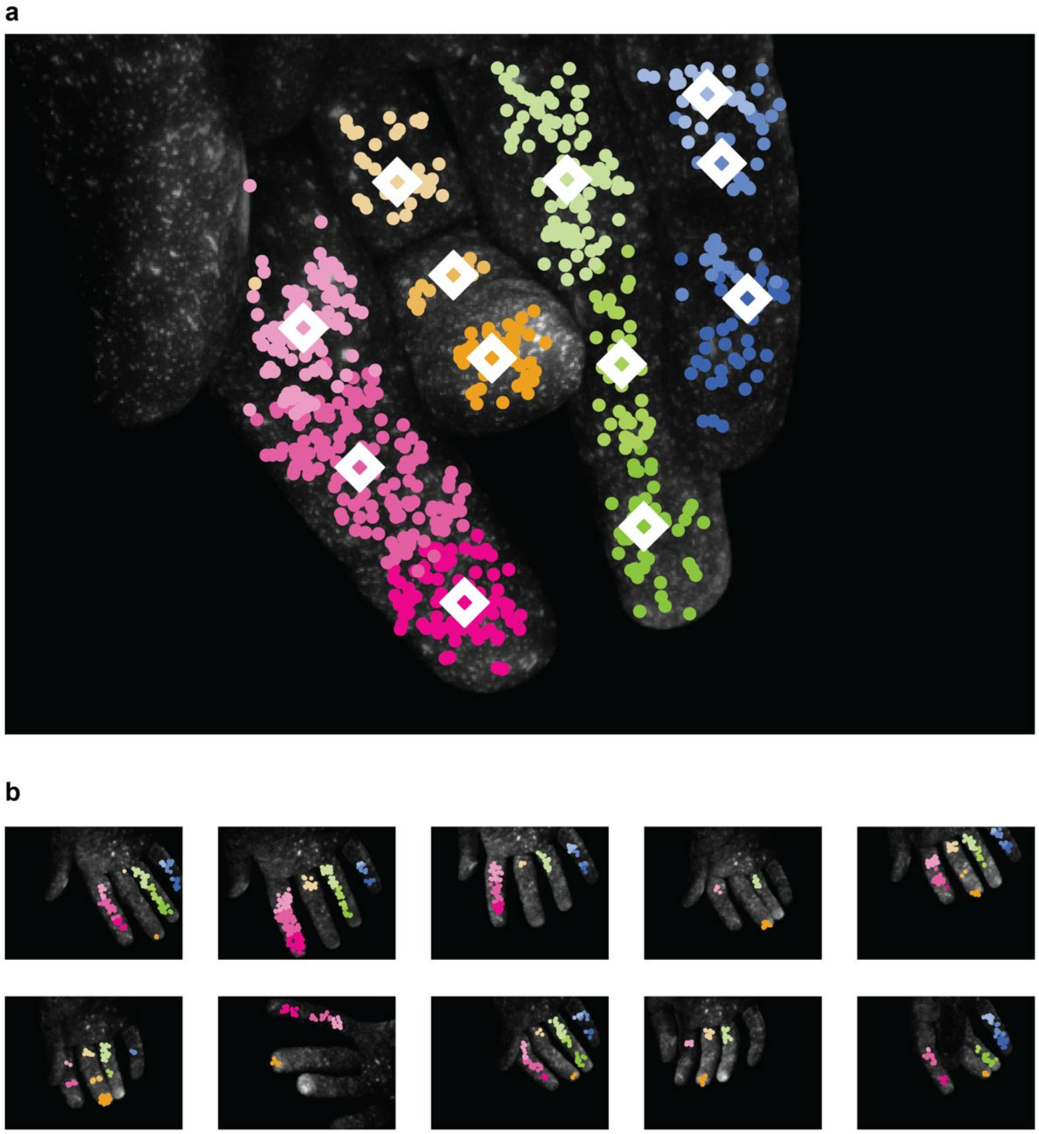

Supp. Fig. 7. Using multiple template images provides more complete coverage. a) A target image with SIFT features (circles) and computed landmark labels (diamonds). Only SIFT features that matched at least one template image in **b** are shown, and color represents the feature's neighborhood membership in the highest-ranked template that it matched. **b)** The 10 template images from which the above target image was labeled. Circles represent matched SIFT features, colored by neighborhood membership. Note that no single template provides coverage of all 12 neighborhoods. Jointly, however, they provide complete coverage.

Training set	**Scale optimization**	**AUC**	**OKS-mAP**	
250 *uniform*	none	0.24	0.49	*Diverse* test set
500 *uniform*	none	0.27	0.52	
1k *uniform*	none	0.33	0.57	
1k *diverse*	none	0.51	0.70	
300k *diverse*	none	**0.89**	**0.95**	
1k *diverse*	none	0.21	0.34	*Challenge* test set
380k *diverse*	none	0.52	0.60	
380k *diverse*	image-level	0.69	0.75	
380k *diverse*	clip-level	**0.76**	**0.82**	

Supp. Table 1. Neural network evaluation with the OKS-mAP metric yields similar results as AUC. The object keypoint similarity mean average precision (OKS-mAP; last column) is another standard performance metric developed for human keypoint evaluation. The metric ranges from 0 to 1, with 1 representing the best possible performance. Each row represents a trained neural network model. The top section represents results on the *diverse* test set (AUC values reproduced from **Fig. 3**), while the bottom section represents results on the *challenge* test set (AUC values reproduced from **Fig. 4**). The OKS-mAP metric yields similar results as the AUC metric.

Supp. Video 1. Screencast of video capture software with visible light and UV frames displayed side-by-side. Real-time image capture software while recording a mouse with hidden fluorescent dye on its left hand. The left and right image feeds show the visible and UV illumination frames respectively (i.e., each feed shows only alternate frames). The bottom panel shows information about the video clips that have been captured so far. The far-left panel controls the timing of the different phases of the imaging and illumination cycle.

Supp. Video 2. Video of capture rig in operation, slowed down 10x to reveal active illumination source cycling among LED clusters. The capture rig during video recording. Video (10x speed) shows how the active illumination source cycles among the nine lighting clusters. All UV sources on the lower five lighting clusters are active simultaneously (they appear out-of-sync due to rolling shutter).

Supp. Video 3. Deep learning model trained on hidden fluorescent labels tracks the hand of an unlabeled mouse. Output predictions from a deep learning model trained to detect the left hand of the mouse. Confidence score is also shown. The reaching behavior was seen during training, but the lighting and camera setup are novel.

Supp. Video 4. Training data generated using massively parallel visual barcoding. Training data generated using massively parallel labeling with visual barcodes and the manual neighborhood selection pipeline. Both UV and visible images were captured, but for clarity only the visible images are shown. Each dot represents a SIFT match between the given video frame and a template image; dot color encodes which finger segment the match corresponds to in the template. Each diamond represents the centroid of all matches corresponding to a particular finger segment. The images along the bottom are the 10 template images.

Supp. Video 5. Deep learning model trained with fluorescent barcoding and manual neighborhood selection tracks the segments of human fingers. Output predictions from a deep learning model trained to detect the finger segments on an unlabeled human hand using the manual neighborhood selection pipeline (training data shown in **Supp. Video 4**). Occluded finger segments do not receive a label.

Supp. Video 6. Deep learning model trained with fluorescent barcoding and automatic neighborhood selection tracks 50 unique landmarks. Output predictions from a deep learning model trained to detect 50 landmarks on first digit of an unlabeled human hand using the automatic neighborhood selection pipeline.